Bifurcations in the Echebarria-Karma Modulation Equation for Cardiac Alternans in One Dimension

by

Shu Dai

Department of Mathematics
Duke University

Date: _____

Approved:

_____
David G. Schaeffer, Advisor

_____
J. Thomas Beale

_____
Harold E. Layton

_____
Michael C. Reed

Dissertation submitted in partial fulfillment of the requirements for the degree of
Doctor of Philosophy in the Department of Mathematics
in the Graduate School of Duke University
2009

Abstract

(Mathematics)

Bifurcations in the Echebarria-Karma Modulation Equation for Cardiac Alternans in One Dimension

by

Shu Dai

Department of Mathematics
Duke University

Date: _____

Approved:

_____
David G. Schaeffer, Advisor

_____
J. Thomas Beale

_____
Harold E. Layton

_____
Michael C. Reed

An abstract of a dissertation submitted in partial fulfillment of the requirements for the degree of Doctor of Philosophy in the Department of Mathematics in the Graduate School of Duke University
2009

Abstract

While alternans in a single cardiac cell appears through a simple period-doubling bifurcation, in extended tissue the exact nature of the bifurcation is unclear. In particular, the phase of alternans can exhibit wave-like spatial dependence, either stationary or travelling, which is known as *discordant* alternans. We study these phenomena in simple cardiac models through a modulation equation proposed by Echebarria-Karma. In this dissertation, we perform a bifurcation analysis for their modulation equation.

Suppose we have a cardiac fiber of length ℓ, which is stimulated periodically at its $x = 0$ end. When the pacing period (basic cycle length) B is below some critical value B_c, alternans emerges along the cable. Let $a(x, n)$ be the amplitude of the alternans along the fiber corresponding to the n-th stimulus. Echebarria and Karma suppose that $a(x, n)$ varies slowly in time and it can be regarded as a time-continuous function $a(x, t)$. They derive a weakly nonlinear modulation equation for the evolution of $a(x, t)$ under some approximation, which after nondimensionalization is as follows:

$$\partial_t a = \sigma a + \mathbf{L}a - ga^3, \tag{1}$$

where the linear operator

$$\mathbf{L}a = \partial_{xx}a - \partial_x a - \frac{1}{\Lambda}\int_0^x a(x', t)dx'.$$

In the equation, σ is dimensionless and proportional to $B_c - B$, i.e., σ indicates

how rapid the pacing is, Λ^{-1} is derived from the conduction velocity (CV) of the propagation, and the nonlinear term $-ga^3$ limits growth after the onset of linear instability. No flux boundary conditions are imposed on both ends.

The zero solution of their equation may lose stability as the pacing rate is increased. To study the bifurcation, we calculate the spectrum of operator $\mathbf{L}$. We find that both a Hopf and a steady-state bifurcation occur. Which bifurcation occurs first depends on parameters in the equation, and for one critical case both modes bifurcate together at a degenerate (codimension 2) bifurcation.

For parameters close to the degenerate case, we investigate the competition between modes, both numerically and analytically. We find that at sufficiently rapid pacing (but assuming a 1:1 response is maintained), steady patterns always emerge as the only stable solution. However, in the parameter range where Hopf bifurcation occurs first, the evolution from periodic solution (just after the bifurcation) to the eventual standing wave solution occurs through an interesting series of secondary bifurcations.

We also find that for some extreme range of parameters, the modulation equation also includes chaotic solutions. Chaotic waves in recent years have been regarded to be closely related to dreadful cardiac arrhythmia. Proceeding work illustrates some chaotic phenomena in two- or three-dimensional space, for instance spiral and scroll waves. We show the existence of chaotic waves in one dimension by the Echebarria-Karma modulation equation for cardiac alternans. This new discovery may provide a different mechanism accounting for the instabilities in cardiac dynamics.

To My Parents

Contents

List of Tables

List of Figures

Acknowledgements

This dissertation would not have been possible without the support and guidance of Dr. David G. Schaeffer. I would like to express my gratitude and appreciation to him for his encouragement, directing and friendship in the past five years.

I am greatly indebted Professor Henry S. Greenside for his fruitful suggestions regarding chaos. I would like to thank Professor John A. Trangenstein, Professor Daniel J. Gauthier and Professor Wanda Krassowska for useful discussions. I would like to thank Professor J. Thomas Beale and Professor Stephanos Venakides for the time I was with them at Duke. I also acknowledge Professor Harold E. Layton and Professor Michael C. Reed for being in my committee and proofreading the dissertation. I would like to thank Professor Mark L. Huber and Professor Thomas P. Witelski for their help in my graduate study. I am also very grateful to Professor Lewis D. Blake for his guidance in my teaching career at Duke.

I wish to thank the fellow graduate students at Duke and my friends for their friendship and help. In particular I want to thank Rann Bar-On, Matthew M. Bowen, John W. Cain, Kevin E. Gonzales, Aubrey R. HB, Aaron D. Jackson, Botao Jia, M. George Lam, Anna V. Little, Shishi Z. Luo, Xiaoxian Luo, David E. Rose, S. Jane Schott, Abaraham D. Smith, Rachel L. Thomas, Jason R. Wilson and Feng Xu.

I also want to express my gratefulness to my wife for her support and understanding during the time.

Finally, this dissertation is dedicated to my parents.

1

Introduction

The heart is a vital organ pumping blood containing oxygen and nutrients to the body. Pumping is the result of a rhythmic cycle of contraction and relaxation of a large number of cardiac cells. If the normal rhythm of the beating is disrupted, the condition is called cardiac arrhythmia. Some arrhythmias are life-threatening and can result in heart attack and sudden death. As ventricular fibrillation (a fatal arrhythmia) accounts for 1/6 of all the deaths in United States [54, 59], it is important to understand these phenomena.

In the past few decades, researchers set up many mathematical models to describe the activity of the cardiac cells [5, 18, 29, 36, 37, 38, 41, 45, 61]. The general equation for the membrane potential V of a single cardiac cell is provided by the electrical circuit model in the following form [33]:

$$C_m \frac{dV}{dt} + I_{\text{ion}}(V, t) = 0. \tag{1.1}$$

In the equation, V is the membrane potential of the cell which may vary with time, C_m is a constant denoting the electrical capacitance per unit area of the cell membrane and I_{ion} is the overall transmembrane ionic current per unit area. Specifics

for the determination of I_{ion} are provided in the following subsections. Our goal is to mathematically analyze the dynamics implied, especially when spatial effects are considered. To begin, we introduce some concepts from physiology.

1.1 Electrical Properties of a Single Cell

Normally a heart beats $60 \sim 80$ times in one minute. The timing of contractions is controlled by electrical signals. The signal is initiated in a cluster of cells called sinoatrial node (SA node) in the right atrium and propagated through the heart in a two-stage process. In each beat, the contraction of muscle cells is initiated by the arrival of the signal. The propagation process, the details of which can be found in [40], is described briefly below. First, the signal propagates throughout the atrial cells and atrial cells contract. The atria and ventricles are "insulated" from each other except along a pathway called atrioventricular node (AV node), which allows the signal to continue its propagation after a brief delay. After the delay, the signal propagates through two bundle branches composed of Purkinje fibers consisting of special type of cells. The tree-like Purkinje fiber network enables the signal to spread quickly over the ventricular cells, causing the ventricles to contract. Figure 1.1 shows a schematic diagram of the cardiac conduction system.

In atria and ventricles, the cardiac cells are roughly cylindrical in shape with approximately diameter of 15μm and length of 100μm. The membrane potential V in (1.1) is the voltage across walls of cells, which in the usual convention is defined as the intracellular potential ϕ_i minus the extracellular potential ϕ_e, i.e.,

$$V = \phi_i - \phi_e. \tag{1.2}$$

The transmembrane potential V determines the activity of the cell. The ionic current I_{ion} in (1.1) is from ions crossing the cell wall. The main contributing ions are K^+, Na^+ and Ca^{2+}, which are contained in both the intracellular and extracellular spaces

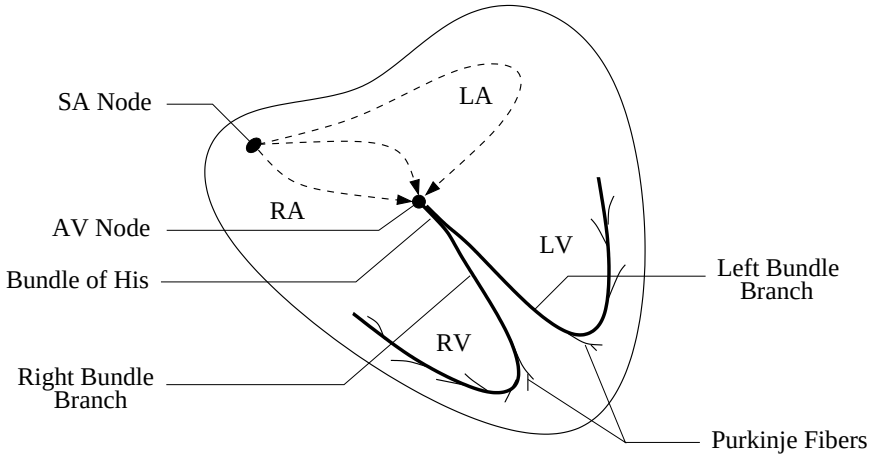

FIGURE 1.1: A schematic view of the conduction system of the heart . The signal is initiated in the SA node and activates the atria, then the signal propagates to the ventricles through the AV node.

of the cell. The internal and external concentrations of each type of ions are very different in general. The membrane of the cell, which separates the cytoplasm and external environment, is selectively permeable. There are large numbers of different types of selective channels for the ions to pass through in the membrane; for instance the sodium channels only allow the sodium ions to pass through.

For a given type of ion and one corresponding selective channel in the membrane, in most cases the channel may be in three states: open, closed, and inactivated (in some simplified models, the channel may only have two states: open and closed). When the channel is open, the ions in the channel are driven by two forces: (1) the diffusive "force" due to the difference between intracellular and extracellular concentrations and (2) the electric force due to the membrane potential. There is a particular value of the transmembrane potential so that in the channel the two forces are balanced, which is called the *Nernst potential*. The Nernst potential for ions of type p may be calculated by the following formula,

$$V_p = \frac{RT}{zF} \ln \frac{c_{p,e}}{c_{p,i}}, \tag{1.3}$$

Table 1.1: Typical ion concentrations and Nernst potentials in cardiac cells.

Ion	Extracellular (mM)	Intracellular (mM)	Nernst Potential (mV)
Na^+	145	15	60
Cl^-	100	5	-80
K^+	4.5	160	-95
Ca^{2+}	1.8	10^{-4}	130
H^+	10^{-4}	2×10^{-4}	-18

where $R = 8.31\ \mathrm{J} \cdot \mathrm{K}^{-1} \cdot \mathrm{mol}^{-1}$ is the universal gas constant, T is the absolute temperature, z is the charge of the ion, $F = 96485\ \mathrm{C} \cdot \mathrm{mol}^{-1}$ is the Faraday constant, $c_{p,e}$ and $c_{p,i}$ are the extracellular and intracellular concentrations of the ion. If the transmembrane potential V is not at V_p, then the current through the single open channel, i_p is nonzero. The relationship between i_p and V can be modelled in many different ways. One convenient way is to assume the ion current across the membrane is in the following form as a kind of Ohm's law:

$$i_p = g_{p,o}(V - V_p), \tag{1.4}$$

where $g_{p,o}$ is the conductance of a single open channel. Table 1.1 shows typical ionic concentrations in most human cardiac cells (the unit is milimole per liter) and the Nernst potentials corresponding to each type of ion are also provided in the table. A more sophisticated model based on the assumption that the electric field is a constant along the channel suggests the Goldman-Hodgkin-Katz (GHK) equation, the details of which can be found in [33]. In the following, equation (1.4) is preferred and the GHK equation is not used.

For each single channel, ions can pass through only when the channel is open. In the cell membrane, the number of open channels (in stochastic models, the total number of channels times the probability that a channel is open) varies with the membrane potential and time. Therefore the total current of the ion p can be

formulated as the following:

$$I_p = g_p \cdot (V - V_p), \tag{1.5}$$

where I_p is the current per unit area (ionic flux) for type p ion and g_p is the conductance of the membrane per unit area, i.e., $g_p = n \cdot g_{p,o}$, where n is the number of open channels per unit area.

With the consideration of all contributing ions and channels in the membrane, the total current per unit area I is given by

$$I = \sum_p I_p = \sum_p g_p \cdot (V - V_p). \tag{1.6}$$

If I is zero, then the membrane potential is said to be at rest. The *resting potential* can be obtained from (1.6) by setting $I = 0$:

$$V_{\text{rest}} = \frac{\sum_p g_p V_p}{\sum_p g_p}. \tag{1.7}$$

For the human cardiac ventricular cells, the resting potential is approximately $-85\,\text{mV}$. When the membrane potential is at rest, the total current is zero, however, the ionic flux for each type of ion may be nonzero.

The concentration of the ions is maintained by other mechanisms of ion transport, for instance by exchangers and pumps. The currents they contribute are usually small and vary slowly and they may be neglected. A more thorough discussion of transmembrane currents can be found in [33].

If the membrane potential V is not at the its resting value V_{rest}, the net ionic current I is nonzero. The ionic flow then will have an effect on the membrane potential. The evolution of V is modelled by the circuit equation (1.1). In the next section, we discuss a phenomenon in the cardiac cells called *action potential* when V is shifted away from its resting value by an external stimulus.

1.2 Action Potentials in a Single Cardiac Cell

The most important property of cardiac cells is excitability, described as follows. Suppose the cell is initially at rest, i.e., the membrane potential is at the rest value. If an external electrical stimulus (strong enough but short) is applied to the cell, the membrane potential increases and remains at a high level for a substantial interval (usually a few hundreds of milliseconds) and then eventually returns to its rest value. This process is called an *action potential*, and cardiac cells are said to be *excitable*. Excitable cells include not only cardiac cells but skeletal muscle cells and most neurons.

The shape of the membrane potential with respect to time during an action potential varies for different species of cells. Figure 1.2 shows a sketch of the evolution of the membrane potential for cardiac ventricular cells in an action potential. There are four phases: (1) Upstroke, the membrane potential increases sharply; (2) Plateau, the potential keeps at a high level; (3) Repolarization, the potential drops to its resting value; (4) Refractory, the cell approaches its resting state and waits for the next simulation.

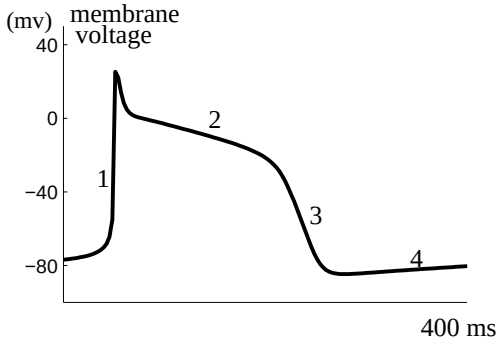

FIGURE 1.2: A typical action potential in the ventricular cells, simulated by the Noble model [45]. There are four phases: 1) upstroke, 2) plateau, 3) repolarization, 4) refractory, as labelled in the picture.

There have been numerous models describing the dynamics of the action poten-

tial for excitable cells of various species. The general construction of the models requires specifying the constituent ions of the current $I_{\text{ion}}(V, t)$. The first model for the action potential was given by Hodgkin and Huxley [26] for the squid giant axon which contained one inward sodium current (fast) and one outward potassium current (slow). For cardiac cells, the first model was constructed by Noble [45], which described the action potential of the Purkinje fiber cells. It considered a sodium current, two potassium currents and a leak current contributed by anions, typically the chloride. See Figure 1.2 for its shape. Many other ionic models were developed in the past decades, e.g., the Beeler-Reuter model in 1977 [5], which described the electrical activity of ventricular myocardial cells, considered four ionic currents including a calcium current accounting for the contractile machinery of the heart. The Luo-Rudy I model in 1991 [36], a generalization of the Beeler-Reuter model, is another classical model for ventricular cells. The above models are sometimes called models of the first generation. In 1994, Luo and Rudy published the Luo-Rudy II model [37], which was a substantial improvement of their 1991 model. The new model described twelve membrane currents in detail and gave a complete description of intracellular ionic concentrations, especially the calcium dynamics in the cytoplasm, junctional sarcoplasmic reticulum (JSR), and network sarcoplasmic reticulum (NSR). Models like Luo-Rudy II, which describes the evolution of intracellular calcium concentration (mainly in the SR), are said to be of the second generation. For those more advanced models, the ionic currents are usually very complicated and include a large number of currents. More models have been developed recently for cardiac cells of different types [29, 38, 53, 61].

The models introduced above are mainly constructed to match experimental results in detail. There are also a number of mathematical models, which qualitatively describe the evolution of the membrane potential during an action potential, but that are simplified and easier to analyze. For example, the FitzHugh-Nagumo model

[16, 17, 44], the two-variable model [31] and the three-current model [15]. In the next section we will look into the details of the action potential in a single cell by using yet another mathematical model called the two-current model, which was proposed by Mitchell and Schaeffer [43].

1.3 The Two-current Model

A single heart cell in the two-current model is described by two dimensionless functions of time, a scaled voltage v and a gate h, that satisfy a set of ODE's

$$\frac{dv}{dt} + J_{\text{ion}}(v,h) + J_{\text{stim}}(t) = 0, \tag{1.8}$$

where the ionic current consists of an inward current and an outward current (in the unusual convention the outward current has positive sign):

$$J_{\text{ion}}(v,h) = -\frac{h}{\tau_{\text{in}}}v^2(1-v) + \frac{v}{\tau_{\text{out}}}, \tag{1.9}$$

and $J_{\text{stim}}(t)$ is an external current applied repeatedly in brief pulses, and

$$\frac{dh}{dt} = \begin{cases} -\dfrac{h}{\tau_{\text{close}}}, & \text{if } v > v_{\text{crit}}; \\ \dfrac{1-h}{\tau_{\text{open}}}, & \text{if } v < v_{\text{crit}}. \end{cases} \tag{1.10}$$

The values of the scaled voltage v and the gate h are both between 0 and 1, and the gate function h affects the inward current as shown in (1.9). Representative values for the parameters in these equations are given in Table 1.2. Note that K in the table is the diffusion coefficient that appears later when we consider the spatial propagation of action potential.

In the absence of a stimulus current, i.e., $J_{\text{stim}} = 0$, equations (1.8)–(1.10) have a stable equilibrium at $(v,h) = (0,1)$. Suppose this equilibrium is perturbed by

Table 1.2: Representative values for the parameters in the two-current model.

τ_{in}	τ_{out}	τ_{open}	τ_{close}	v_{crit}	K
0.2ms	7ms	50ms	130ms	0.05	0.4 $\text{cm}^2 \cdot \text{s}^{-1}$

a sequence of external stimuli, applied with period B (mnemonic for basic cycle length):

$$J_{\text{stim}}(t) = \begin{cases} v_{\text{stim}}/\delta & \text{if } 0 < t < \delta \pmod{B}, \\ 0 & \text{otherwise,} \end{cases} \tag{1.11}$$

where $\delta \ll \tau_{\text{in}}$ and v_{stim} is not excessively small. Provided this pacing is not too rapid, the stimuli produce action potentials as illustrated in Figure 1.3: i.e., each stimulus, although very brief, triggers an extended rise in the voltage, after which the voltage decays. Let the action potential duration (acronym APD; in mathematical formulae A_n) and diastolic interval (acronym DI; in mathematical formulae D_n) be defined as in the figure; note that $A_n + D_n = B$ for each n, where B is the period or basic cycle length.

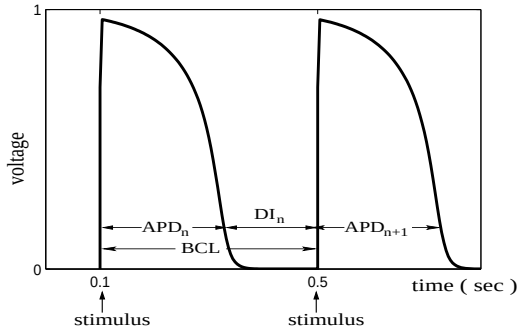

FIGURE 1.3: The solution to ODE system (1.8)–(1.10) with parameters given in the Table 1.2, assuming a periodic stimulus with period BCL = 400ms.

In [43] it is shown that, under the following assumption,

$$\tau_{\text{in}} \ll \tau_{\text{out}} \ll \tau_{\text{open}},\ \tau_{\text{close}}, \tag{1.12}$$

these variables approximately satisfy

$$A_{n+1} = f(D_n), \tag{1.13}$$

where to leading order

$$f(D_n) = \tau_{\text{close}} \ln \left\{ \frac{1 - (1 - h_{\min})\, e^{-D_n/\tau_{\text{open}}}}{h_{\min}} \right\} \tag{1.14}$$

with $h_{\min} = 4\tau_{\text{in}}/\tau_{\text{out}}$. The relationship (1.13) is called the *restitution curve*, first introduced in [46]. Since $D_n = B - A_n$, the sequence A_n is determined by iteration of a one-dimensional map,

$$A_{n+1} = f(B - A_n). \tag{1.15}$$

Note that for the two-current model, equation (1.14) is the leading order approximation for the restitution curve and the next order correction may be significant. For details see [6].

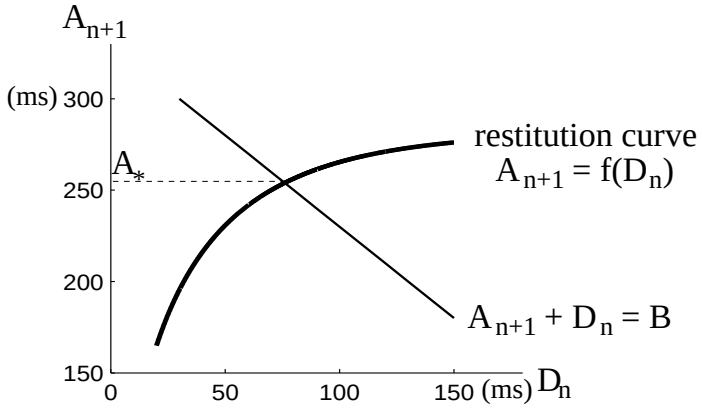

FIGURE 1.4: Graph of the restitution curve given by (1.13) and (1.14). The fixed point solution to the iterated mapping (1.15) for given basic cycle length B can be found by the intersection of the restitution curve $A_{n+1} = f(D_n)$ and the line $A_{n+1} + D_n = B$.

Provided B is not too small, a sequence of A_n generated by (1.15) converges to a stable fixed point $A_*(B)$, as shown in Figure 1.4. However, for B smaller

than some critical value B_c, the fixed point loses its stability and (1.15) exhibits a period doubling bifurcation of A_n, to a response called *alternans*. This behavior also exhibited by the ODE system (1.8)–(1.11). Figure 1.5 is a simulation of ODE system (1.8)–(1.11), which shows an example of alternans with rapid pacing, where the sequence A_n does not converge to a fixed point, but alternates between two distinct values $A_\pm$ after a transient.

We use the mapping model (1.15) to find the critical value B_c of the basic cycle length B for alternans to emerge. Let A_c be the fixed point solution to (1.15) for when B is exactly B_c, and let $D_c = B_c - A_c$. Solving the equation $|f'(D_c)| = 1$, which is the condition for the period-doubling bifurcation [25], we find for the two-current model,

$$D_c = \tau_{open} \ln\left\{(1 - h_{min})(1 + \frac{\tau_{close}}{\tau_{open}})\right\}, \tag{1.16}$$

and thus

$$A_c = f(D_c) = \tau_{close} \ln\left\{\frac{\tau_{close}}{(\tau_{open} + \tau_{close})h_{min}}\right\}. \tag{1.17}$$

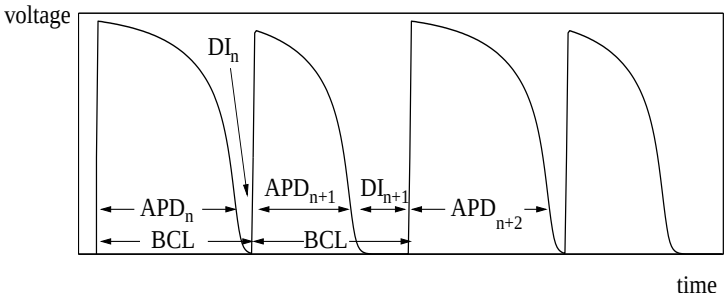

FIGURE 1.5: An illustration of alternans after a long run in case of rapid pacing, obtained by simulating the two-current model with basic cycle length $B = 295$ms and other parameters in Table 1.2.

Let us summarize what we observe in the two-current model. For a single cardiac cell with membrane voltage and gate state evolving according to (1.8)–(1.10) and with asymptotic assumptions in (1.12), given external stimuli with period B, the

action potential duration A_{n+1} is determined by previous diastolic interval D_n by a restitution relationship (1.13). Period-doubling bifurcation occurs when we reduce the basic cycle length B below a critical value B_c and alternans emerges, i.e., in the long run the APD will not converge to a fixed point but alternate between two distinct values. Note that the original ODE system (1.8)–(1.11) has the same behavior. Figure 1.6 is a bifurcation diagram which describes the above results.

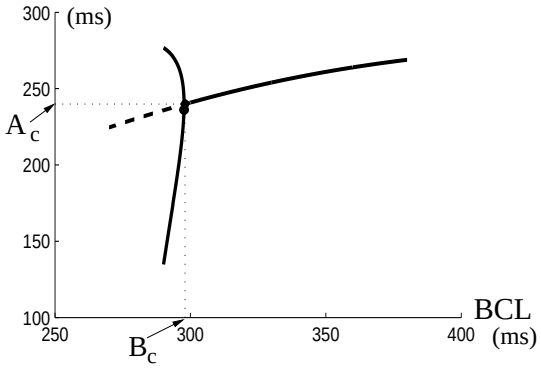

FIGURE 1.6: Bifurcation diagram for the iteration map (1.14)–(1.15), where solid curve represents stability and dashed curve represents instability. As the basic cycle length B decreases, a period-doubling bifurcation occurs at $B_c \approx 295$ ms, the fixed point solution loses its stability, and A_n tends to two distinct values.

For the two-current model, one specific mathematical model for cardiac action potentials, we showed the existence of alternans under rapid pacing. However, this property is universal in the experiments of cardiac cells or general excitable cells. The behavior of other models [1, 15, 31, 43] can also be described by the restitution relationship (1.13). The shape of those restitution curves is similar to the restitution curve of the two current model, which is concave and increasing. A period-doubling bifurcation occurs at the critical value D_c where $f'(D_c) = 1$. In recent years, more terms accounting for memory effects and calcium coupling have been considered to obtain more precise models [8, 13, 52, 53]. However, the following parts in this thesis will be based on the simple case that the action potential duration is determined by

the previous diastolic interval as in (1.13).

1.4 Propagation of Action Potentials Along a Cardiac Fiber

In the cardiac tissue, the cells are packed together surrounded by extracellular medium. A graph indicating the structure of cardiac muscle may be viewed in Figure 9 of [28].

The cells are excitable and connected by gap junctions [39], allowing action potentials to propagate and causing the cells to contract. A straightforward approach for modelling the electrical behavior in extended tissue is to add a diffusion term $K\Delta V$ to the ionic model (1.1). However, a general piece of extended tissue is anisotropic, i.e., it has different electrical properties in different directions in both the intracellular and the extracellular spaces. Researchers find it is convenient to divide the tissue into two separate domains: the intracellular and the extracellular spaces, both of which are assumed to be continuous and fill the complete volume of the heart muscle. Separate equations are given for the intra and extracellular potentials, ϕ_i and ϕ_e. The *bidomain model* was constructed based on the above assumptions [21]. For the formal derivation and details of the model see [33, 56]. In case the extracellular space is assumed to have infinite conductivity, the bidomain model is reduced to the *monodomain model* [57]. In this thesis, we consider only a monodomain model.

Suppose a fiber is formed by placing cardiac cells in a linear array, adjacent cells being connected by gap junctions. The resistance of intracellular cytoplasm is small but the gap junctions usually have a larger resistance. By the technique of homogenization, we may treat the fiber as a uniform continuum with an effective diffusion coefficient. The membrane potential V is regarded as a continuous function of both time and space. The ionic model (1.1) which describes the electrical activity

of a single cell is augmented by a diffusion term:

$$\frac{\partial V}{\partial t} + I_{\text{ion}}(V,t)/C_m = K\frac{\partial^2 V}{\partial x^2}. \tag{1.18}$$

Equation (1.18) is called the *cable equation*. For example, the two-current model on a homogenized cable is obtained by augmenting (1.8) by a diffusion term,

$$\partial_t v = K\partial_{xx} v + J_{\text{ion}}(v,h) + J_{\text{stim}}(x,t); \tag{1.19}$$

equation (1.10) does not acquire any additional terms, but the t-derivative must be reinterpreted as a partial derivative:

$$\frac{\partial h}{\partial t} = \begin{cases} -\dfrac{h}{\tau_{\text{close}}}, & \text{if } v > v_{\text{crit}}; \\ \dfrac{1-h}{\tau_{\text{open}}}, & \text{if } v < v_{\text{crit}}. \end{cases} \tag{1.20}$$

Suppose a stimulus is applied locally near one end of the fiber and vanishes elsewhere. An action potential stimulated near $x = 0$ propagates along the fiber and evolves to a travelling wave, which is observed in both the experiments and simulations of various ionic models. For most realistic ionic models, the current I_{ion} is too complicated to analyze. However, analysis for some mathematical models is possible. For example, in a recent paper [4], it is proved that on an infinite fiber there exists a travelling wave solution to the two-current model for a single pulse.

In case of slow pacing, we expect the membrane potential to converge to a periodic travelling wave train, which is observed in simulations. To find a travelling wave solution, we look for the solution of the form $v = v(\xi)$, where $\xi = x - ct$ for some appropriate travelling speed c, which is called the *conduction velocity*, or CV in abbreviation. For the two-current model, after a calculation which we present in the Appendix A, we find that the conduction velocity of the wave front depends on the

diastolic interval D [43]:

$$c = c(D) \approx \sqrt{\frac{K \cdot h_{\text{ini}}(D)}{2\tau_{\text{in}}}}\Big(1 - \frac{3h_{\min}}{4h_{\text{ini}}(D)}\Big), \tag{1.21}$$

where

$$h_{\text{ini}}(D) = 1 - (1 - h_{\min})e^{-D/\tau_{\text{open}}}. \tag{1.22}$$

The relationship $c = c(D)$ in (1.21) is called the *dispersion curve* [10], which connects the instantaneous propagating speed of the wave front of the action potential and the local diastolic interval.

Assuming the fiber has a finite length ℓ, we impose no-flux boundary conditions at both ends of the fiber:

$$\partial_x v(0,t) = \partial_x v(\ell,t) = 0. \tag{1.23}$$

1.5 Alternans on a Cardiac Fiber

In Section 1.3, by the restitution relationship from the two-current model, we saw alternans in a single cardiac cell emerge through a period doubling bifurcation under rapid pacing. We also discussed the similar mechanism of alternans in general mapping models. The situation becomes more complicated when we consider the extended tissue other than a single cell, for instance a cardiac fiber. As we saw in Section 1.4, action potentials propagate throughout the tissue and each cell is excited when the wave front of each action potential arrives. When the BCL of applied stimuli is sufficiently short, the APD may have a pattern of alternans on the tissue. However, the alternation may have different amplitude at various location and they may even suffer reversal phases.

Figure 1.7 shows the distribution of APDs at two consecutive (odd and even) beats along a cardiac fiber, obtained by simulating the cable equation (1.18) with

Noble's ionic model after a long time run. In the picture, we observe at each location the APD oscillates between two distinct values, however the amplitude of the alternation varies at different location. Furthermore, a crucial feature in Figure 1.7 is that the APD alternates with opposite phases in two or more regions on the fiber, i.e. the APD in one region performs a sequence of $LSLS...$ and $SLSL...$ in the other. This pattern of alternation is known as *discordant alternans* and it has been implicated as a precursor of life-threatening arrhythmia [9, 20, 49, 51]. Therefore great importance attaches to understanding it. We also note that if the alternans on the entire tissue has a uniform phase, then it is called *concordant alternans*.

The discordant alternans shown in Figure 1.7 is said to have a pattern of standing waves, since at every location the amplitude of the oscillation of APD does not vary by time. Figure 2.5 below shows anther possible case when the amplitude of alternans evolves with time in a travelling pattern.

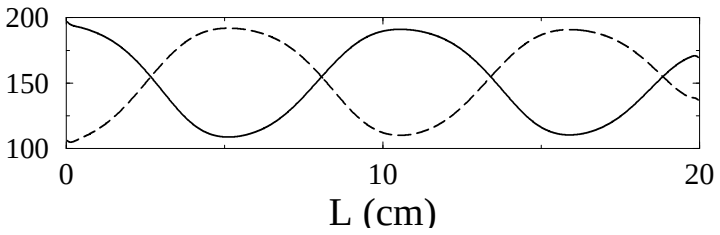

FIGURE 1.7: An illustration of action potential durations at two consecutive (odd and even) beats along a cardiac fiber after a long run, obtained by simulating the cable equation (1.18) with Noble's ionic model for the basic cycle length $B = 258$ms. The simulation is performed by Echebarria and Karma [11].

One might hope to find a travelling wave solution of constant speed in the alternans regime. Unfortunately this type of solution in general does not exist by the following argument. In Section 1.4 we investigated the propagation of action potential along a cardiac fiber, using the two-current model as an example. The conduction velocity, or the travelling speed of wave front of the action potential,

is given in (1.21), which is a function of the previous diastolic interval.[1] However, when alternans emerges, the diastolic interval at every location also alternates in a $LSLS$ or $SLSL$ sequence. Thus the travelling speed of the wave front of each action potential cannot be a constant.

The above argument for the non-existence of travelling wave solution of constant velocity illustrates that it is hard to analytically describe the alternans directly from the reaction-diffusion cable equation (1.18). Echebarria and Karma found an alternative approach. They avoided referring to the detailed form of the ionic models to obtain the APDs, but started from the general mapping model, i.e., the restitution relationship (1.13). They considered the alternans in a one-dimensional homogeneous fiber, the simplest case of extended tissue, and assumed that each cell in the fiber has the same restitution curve. Under some approximations, they proposed a weakly nonlinear modulation equation for the amplitude of the alternans. In the next section we will show their idea and main steps of the derivation. And the goal of this thesis is to explore the implicated mathematics and phenomena in their modulation equation.

1.6 The Echebarria-Karma Modulation Equation

To investigate the evolution of the amplitude of the alternans along a fiber of excitable cells, in their seminal paper [11] Echebarria and Karma derived a weakly nonlinear modulation equation, starting from the general restitution curve (1.13). The derivation consists of two stages. They first neglect the coupling effect between adjacent cells [58] to obtain an evolutionary equation and then modify the equation to include the cell coupling. And this section is a summary of their work.

We consider a cardiac fiber which is paced at one end $x = 0$ with period B. We also assume each stimulus creates an action potential that succeeds to propagate

[1] The conduction velocity may depend on more factors than DI, but it always varies with DI.

to the other end. For every location x (each cell in the practical meaning) on the fiber, the following three variables are used to approximately describe the dynamics: (1) $T(x,n)$, the time interval between the arrival of n-th and $(n+1)$-th action potential at the location x, which plays the same role as the BCL in the single cell model; in particular, $T(0,n) = B$; (2) $A(x,n)$, the APD corresponding to the n-th stimulus at location x; (3) $D(x,n)$, the diastolic interval after the n-th APD.

We set up three main equations below for the above three variables:

$$T(x,n) = A(x,n) + D(x,n), \tag{1.24}$$

$$T(x,n) = B + \int_0^x \frac{dx'}{c(D(x',n))} - \int_0^x \frac{dx'}{c(D(x',n-1))}, \tag{1.25}$$

$$A(x,n+2) = f[T(x,n+1) - f[T(x,n) - A(x,n)]]. \tag{1.26}$$

The first equation (1.24) is obtained directly from the definitions of $A(x,n)$, $D(x,n)$ and $T(x,n)$, where $T(x,n)$ acts as a local cycle length of the n-th stimulus at position x though it is not a constant any more. The second equation (1.25) is derived from the kinetics, in which the first integral on the right-hand side is the time for the wave front of the action potential of n-th stimulus to travel from the paced end to x. The second integral in (1.25) has a similar intepretation for $(n+1)$-th stimulus. The third equation (1.26) is obtained by iteration of the restitution curve (1.13) at every location x, i.e., we assume $A(x,n+1) = f(D(x,n)) = f(T(x,n) - A(x,n))$ for all x and n, which is equivalent to assuming that the coupling effect of adjacent cells is not considered. However, below this effect will actually need to be included.

In case of rapid pacing when the period B is below the critical value B_c, we may have alternans along the fiber. As we discussed in Section 1.3, in case of a single cell for $B < B_c$ the iterated sequence of (1.15) alternates between two distinct values in the long run. Now for a cardiac fiber, the amplitude of alternation may vary with

both location and time and the dynamics of the amplitude is what we are interested in.

Before deriving a dynamical equation from (1.24)–(1.26), we introduce some new variables. $A(x,n)$ and $T(x,n)$ are assumed to perform a alternating pattern for each position x. We define $a_n(x)$ and $b_n(x)$ to be the amplitude of the alternation of $A(x,n)$ and $T(x,n)$ as follows:

$$A(x,n) = A_c - \delta A + (-1)^n a_n(x), \tag{1.27}$$

and

$$T(x,n) = B_c - \delta\tau + (-1)^n b_n(x), \tag{1.28}$$

where $\delta\tau = B_c - B$ and δA is the average shortening of APD resulting from decreasing B below B_c. If B is below but still close to B_c, the amplitudes of the alternation, $a_n(x)$ and $b_n(x)$, are assumed to be small and vary slowly with respect to n. Because of this slow-variation assumption, one may study the evolution of a with respect to a continuous time t that interpolates between the times $t = nB,\ \ n = 0, 1, 2, \ldots$, when stimuli are applied, i.e., we may regard $a_n(x)$ as discrete values of some continuous function $a(x,t)$ at $t = nB$, and also for $b_n(x)$, which is regarded as discrete values of a continuous function $b(x,t)$ at $t = nB$.

As introduced above, $a(x,t)$ denotes the amplitude of the alternation of the action potential duration. The purpose is to obtain a spatiotemporal equation for $a(x,t)$ from the equations (1.24)–(1.26). We show the main steps below.

Substituting (1.27) and (1.28) into (1.24), we obtain an equation describing the amplitude of the alternation of local diastolic interval:

$$D(x,n) = T(x,n) - A(x,n) = D_c + \delta\tau - \delta A + (-1)^n (b - a). \tag{1.29}$$

Thus the travelling speed $c(D(x,n))$ in (1.25) can be linearly approximated around

the critical value D_c as follows:

$$c(D(x,n)) = c + (\delta\tau - \delta A + (-1)^n(b-a)) \cdot c' + \text{higher order terms}, \tag{1.30}$$

where for convenience we use c and c' to denote the conduction velocity and its derivative with respect to the diastolic interval D, both at the critical value, i.e., in equation (1.30) $c = c(D_c)$ and $c' = c'(D_c)$. Substituting (1.30) into (1.25), we find that to the leading order,[2]

$$b(x,t) = \frac{2c'}{c^2}\int_0^x (a(x',t) - b(x',t))\, dx', \tag{1.31}$$

or equivalently

$$\partial_x b(x,t) = \frac{1}{\Lambda}(a(x,t) - b(x,t)), \tag{1.32}$$

with boundary condition $b(0,t) = 0$, where

$$\Lambda = \frac{c^2}{2c'} \tag{1.33}$$

has units of length. And we find

$$b = \frac{1}{\Lambda}\int_0^x e^{\frac{1}{\Lambda}(x'-x)} a(x',t)dy \approx \frac{1}{\Lambda}\int_0^x a(x',t)dx', \tag{1.34}$$

where the approximation is applied when $|x|$ is much smaller than the scale of Λ, and then $b(x,t)$ is much smaller than $a(x,t)$. Equation (1.34) gives a relationship between the amplitude of the alternations of local action potential duration and effective local cycle length.

The third equation (1.26) specifies the temporal variation of the action potential duration. Applying perturbation theory, we find

$$A(x,n+2) - A(x,n) = a(x,(n+2)B) - a(x,nB) \approx 2B\partial_t a(x,nB) = 2B\partial_t a(x,t). \tag{1.35}$$

[2] In fact we can only have (1.31) and (1.32) at discrete times $t = nB$ since the perturbation formula (1.29) is given only at these discrete times. We assume (1.31) and (1.32) can be generalized to all times by interpolation.

Thus (1.26) and (1.35) imply that to the lowest order

$$2B\partial_t a(x,t) = f[T(x,n+1) - f[T(x,n) - A(x,n)]] - A(x,n). \tag{1.36}$$

We then consider the expansion of the right hand side of (1.26) for $T(x,n)$ and $A(x,n)$ to the lowest order about the critical values B_c and A_c respectively, provided (1.28) and (1.27). As shown in the Appendix B, we find that to leading order

$$B\partial_t a(x,t) = \sigma a(x,t) - ga^3 - \frac{1}{\Lambda}\int_0^x a(x',t)dx', \tag{1.37}$$

where

$$\sigma = \frac{\delta\tau \cdot f''}{2} \tag{1.38}$$

and

$$g = \frac{f''^2}{4} - \frac{f'''}{6}. \tag{1.39}$$

Note that all the derivatives of $f(D)$ in (1.38) and (1.39) are taken at the critical value D_c. In the derivation of the modulation equation, $b(x,t)$ is assumed to be much smaller than $a(x,t)$ in magnitude and $\delta A \approx \delta\tau/2$ is also assumed to be much smaller than $a(x,t)$.

However, equation (1.37) *leads to untenable predictions.* Echebarria and Karma observed by numerical simulation that the solution to (1.37) evolves to have unphysical spatial discontinuities [11]. This can be cured by considering the cell coupling effect. They argued in [12] that the coupling effect contributes additional diffusion and convection terms in the right hand side of (1.37), and they obtained the modulation equation below:

$$B\partial_t a = \sigma a + \xi^2\partial_{xx}a - w\partial_x a - ga^3 - \frac{1}{\Lambda}\int_0^x a(x',t)dx', \tag{1.40}$$

where the constants w and ξ are given by

$$w = 2K/c, \quad \xi = \sqrt{KA_c} \tag{1.41}$$

Note that in (1.41) K is the diffusion coefficient in the cable equation (1.18) and $c = c(D_c)$ is the conduction velocity at the critical value. Neumann boundary conditions are imposed at the two ends of the fiber:

$$\partial_x a(0,t) = 0, \quad \partial_x a(\ell,t) = 0. \tag{1.42}$$

1.7 Organization of the Dissertation

In the following chapters, we focus on the dynamics of the modulation equation (1.40), which has a trivial zero solution. The trivial solution may lose stability through bifurcation as σ increases (or equivalently the pacing rate increases). In Chapter 2, to investigate the linear stability of the zero solution, we consider the spectrum of the linearized operator of the spatial part of the equation. We find that there are two different modes: Hopf and steady-state. The bifurcation we first encounter as σ increases is determined by which mode loses stability first. By adjusting parameters we in fact have a codimension-two bifurcation. In Chapter 3, we discuss the mode competition about the degenerate case when the two modes lose stability simultaneously and perform bifurcation analysis for parameters close to the degenerate case. In Chapter 4, we investigate a chaotic solution we observe from the modulation equation for some extreme values of the parameters and verify the existence of chaos by numerical computation. Chapter 5 is the conclusion and discussion.

2

Spectrum of the Linearized Operator

Suppose a cardiac fiber of length ℓ is stimulated periodically with period B at its $x = 0$ end. We assume that each stimulus successfully generates an action potential that propagates down the fiber. As we introduced in Chapter 1, Echebarria and Karma proposed a weakly nonlinear description of the one-dimensional evolution of discordant alternans in one-dimensional cardiac models:

$$\partial_t a = \sigma a + \xi^2 \partial_{xx} a - w \partial_x a - \frac{1}{\Lambda} \int_0^x a(x', t) dx' - g a^3, \tag{2.1}$$

where the time is scaled over the basic cycle length B; and $a(x, t)$ is the amplitude of alternans introduced in (1.27), σ is the bifurcation parameter, which is proportional to $B_c - B$; Λ, w, and ξ are all positive parameters in units of length, which are derived from the equations of the cardiac model; and the nonlinear term $-ga^3$ limits growth after the onset of linear instability. Boundary conditions (B.C.s)

$$\partial_x a(0, t) = 0, \quad \partial_x a(\ell, t) = 0 \tag{2.2}$$

are imposed on (2.1). Of course, $a \equiv 0$ is a solution of (2.1)–(2.2), but it loses stability as σ increases. Bifurcation analysis of this equation requires knowing the

eigenvalues Ω_n of the linear operator that maps a function $a(x)$ to

$$\xi^2 \partial_{xx} a - w \partial_x a - \frac{1}{\Lambda} \int_0^x a(x', t) dx', \tag{2.3}$$

subject to Neumann boundary conditions. All of these eigenvalues lie in the (stable) left-half plane. The eigenvalue(s) with the largest real part, say $\Omega_{\max}$, determines the character of the solution of (2.1) at the onset of bifurcation—a stationary pattern if $\Omega_{\max}$ is real, a moving pattern if it is complex.

In this chapter we extend the results of Echebarria and Karma by calculating the spectrum of (2.3) with purely analytical means in two limiting cases: small dispersion and a long fiber. In particular, it follows from our analysis that in a long fiber $\Omega_{\max}$ is real if, modulo terms that are $\mathcal{O}(\ell^{-2})$,

$$\Lambda^{-1} \leq C \frac{w^3}{\xi^4}, \tag{2.4}$$

where

$$C = \frac{1}{64} \left(71 + 17\sqrt{17} \right) \approx 2.205, \tag{2.5}$$

and $\Omega_{\max}$ is complex otherwise.

2.1 The Eigenvalue Problem

Let us begin by nondimensionalizing (2.3). The parameters ξ, w, and Λ, like ℓ, all have the units of length. Thus we define a set of new parameters

$$\bar{w} = w \cdot \xi^{-1}, \quad \bar{\Lambda} = \Lambda \cdot w^3 \xi^{-4}, \quad \bar{x} = x \cdot w\, \xi^{-2}, \quad \bar{\ell} = \ell \cdot w\, \xi^{-2}, \tag{2.6}$$

and an operator

$$\mathbf{L}a = \frac{d^2 a}{d\bar{x}^2} - \frac{da}{d\bar{x}} - \bar{\Lambda}^{-1} \int_0^{\bar{x}} a(\bar{x}') d\bar{x}'. \tag{2.7}$$

One observes that (2.3) equals $\bar{w}^2 \cdot \mathbf{L}a$.

The analysis in sections 2.1–2.3 below uses dimensionless variables, but we nonetheless *shall omit all the bars* in (2.7). Suppose that $a(x)$ is an eigenfunction of (2.7) with eigenvalue Ω: i.e.,

$$\mathbf{L}a = \Omega\, a, \quad \text{with} \quad \mathrm{a}'(0) = 0, \quad \mathrm{a}'(\ell) = 0. \tag{2.8}$$

To eliminate the integral term in (2.7), we differentiate this equation (but not the boundary conditions) with respect to x to obtain

$$\begin{cases} a''' - a'' - \Lambda^{-1} a = \Omega\, a', \\ a'(0) = 0, \\ a'(\ell) = 0, \\ a''(0) = \Omega\, a(0). \end{cases} \tag{2.9}$$

The additional B.C. comes from evaluating the eigenvalue equation, before differentiation, at $x = 0$. A function of the form $a(x) = e^{\kappa x}$ satisfies the ODE in (2.9) if

$$\kappa^3 - \kappa^2 - \Omega\kappa - \Lambda^{-1} = 0. \tag{2.10}$$

If $\kappa_1, \kappa_2, \kappa_3$ are the roots of (2.10), then this equation may be reformulated as

$$1 = \kappa_1 + \kappa_2 + \kappa_3, \tag{2.11}$$

$$\Omega = -(\kappa_1\kappa_2 + \kappa_2\kappa_3 + \kappa_3\kappa_1), \tag{2.12}$$

$$\Lambda^{-1} = \kappa_1\kappa_2\kappa_3. \tag{2.13}$$

Assuming that the roots κ_1, κ_2, κ_3 are distinct, we seek a solution of (2.9) of the form $a(x) = \sum_1^3 C_i e^{\kappa_i x}$. The three B.C.s in (2.9) give a homogeneous linear system for the unknown coefficients C_i. For this system to possess a nontrivial solution, we need

$$\det \begin{pmatrix} \kappa_1 & \kappa_2 & \kappa_3 \\ \kappa_1 e^{\kappa_1 \ell} & \kappa_2 e^{\kappa_2 \ell} & \kappa_3 e^{\kappa_3 \ell} \\ \Omega - \kappa_1^2 & \Omega - \kappa_2^2 & \Omega - \kappa_3^2 \end{pmatrix} = 0. \tag{2.14}$$

Thus $\Omega \in \mathbb{C}$ is an eigenvalue of $\mathbf{L}$ if there exist a triple κ_1, κ_2, κ_3, no two of them equal, such that the four equations (2.11)–(2.14) are satisfied.

If $\Lambda^{-1} > 0$ so that each root κ_i is nonzero, (2.14) may be reformulated as follows. By (2.10), $\Omega - \kappa_i^2 = -\kappa_i - \Lambda^{-1}\kappa_i^{-1}$. Substituting this expression into the third row of (2.14) and manipulating the determinant, we obtain

$$\det \begin{pmatrix} 1 & 1 & 1 \\ e^{\kappa_1 \ell} & e^{\kappa_2 \ell} & e^{\kappa_3 \ell} \\ \kappa_1^{-2} & \kappa_2^{-2} & \kappa_3^{-2} \end{pmatrix} = 0. \tag{2.15}$$

Let us rule out possible multiple roots. First consider a triple root, which by (2.11) must be $\kappa_1 = \kappa_2 = \kappa_3 = \frac{1}{3}$: In this case the general solution to (2.9) is of the form $a(x) = (C_0 + C_1 x + C_2 x^2)\, e^{x/3}$, and the only possible eigenvalue is $\Omega = -\frac{1}{3}$ by (2.12). Substituting $a(x)$ and Ω into (2.9), we find that there is no nontrivial solution and hence no eigenvalue.

Now we assume $\kappa_1 = \kappa_2 \neq \kappa_3$ in (2.11)–(2.13), and therefore the general solution to (2.9) is $a(x) = C_1 e^{\kappa_1 x} + C_2 x e^{\kappa_1 x} + C_3 e^{\kappa_3 x}$. Inserting $a(x)$ into the boundary conditions in (2.9) and considering (2.11)–(2.13) with $\kappa_2 = \kappa_1$, we find that the existence of a nontrivial solution requires κ_1 to satisfy both of the following equations,

$$\kappa_1 \ell (4\kappa_1^2 - 3\kappa_1 - 1) + 2(1 - 2\kappa_1)^2 \cdot \left[e^{(1-3\kappa_1)\ell} - 1 \right] = 0, \tag{2.16}$$

$$-2\kappa_1^3 + \kappa_1^2 = \Lambda^{-1} > 0, \tag{2.17}$$

and the possible eigenvalue is then given by

$$\Omega = 3\kappa_1^2 - 2\kappa_1. \tag{2.18}$$

Note that (2.16) only has isolated complex roots since its left-hand side is a holomorphic function. Thus (2.16)–(2.18) can provide only isolated eigenvalues in the Λ^{-1}-Ω plane, and a perturbation of the parameter Λ^{-1} will lead to the case when all κ_j's are different. So the case $\kappa_1 = \kappa_2 \neq \kappa_3$ can be obtained as limit of cases with distinct roots.

2.2 Small Dispersion

We remind the reader that in this section, Λ and ℓ, without bars, refer to the dimensionless parameters defined by (2.6).

If $\Lambda^{-1} = 0$, then $\mathbf{L}$ has first eigenvalue

$$\Omega_0^{(0)} = 0, \tag{2.19}$$

with the solution of (2.11)–(2.13) given by $\kappa_j = 0,\ 0,\ 1$, and later eigenvalues

$$\Omega_n^{(0)} = -\frac{1}{4} - \left(\frac{\pi n}{\ell}\right)^2, \qquad n = 1, 2, \ldots \tag{2.20}$$

with $\kappa_j = 0,\ \frac{1}{2} \pm \frac{in\pi}{\ell}$. We seek the first term in an expansion of Ω_n in powers of Λ^{-1}.

2.2.1 Perturbation of Ω_0

We prove that for Λ^{-1} small,

$$\Omega_0(\Lambda) = \Omega_0^{(1)}\Lambda^{-1} + \mathcal{O}(\Lambda^{-2}), \tag{2.21}$$

where

$$\Omega_0^{(1)} = -\Big(1 - \frac{\ell}{\exp(\ell) - 1}\Big). \tag{2.22}$$

For $\Lambda^{-1} = 0$, $\kappa_1 = \kappa_2 = 0$ is a double root of (2.11–2.13). Thus we seek a Puisseux expansion [32]:

$$\begin{cases} \kappa_{1,2} = a_{1,2}\Lambda^{-1/2} + b_{1,2}\Lambda^{-1} + \mathcal{O}(\Lambda^{-3/2}), \\ \kappa_3 = 1 + b_3\Lambda^{-1} + \mathcal{O}(\Lambda^{-2}), \\ \Omega_0 = \Omega_0^{(1)}\Lambda^{-1} + \mathcal{O}(\Lambda^{-2}). \end{cases} \tag{2.23}$$

First we substitute into (2.11)–(2.13); from the vanishing of the first two terms in the expansions we deduce

$$\begin{cases} a_1 + a_2 = 0 \\ b_1 + b_2 + b_3 = 0 \\ \Omega_0^{(1)} = -a_1a_2 - (b_1 + b_2) \\ a_1a_2 = 1 \\ a_1b_2 + a_2b_1 = 0. \end{cases} \tag{2.24}$$

Note that the equation $a_1 + a_2 = 0$ arises from the leading term of both (2.11) and (2.12). These equations imply that

$$\begin{cases} a_{1,2} = \pm i \\ b_2 = b_1 \\ b_3 = -2b_1 \\ \Omega_0^{(1)} = -1 - 2b_1. \end{cases} \tag{2.25}$$

Then we substitute (2.25) into the determinant (2.14). The leading term in the resulting expansion, which is $\mathcal{O}(\Lambda^{-1})$, vanishes. Requiring the $\mathcal{O}(\Lambda^{-3/2})$ term to vanish yields the claim (2.22), even though we do not yet know the b_j's.

Incidentally, if desired, the b_j's may be determined by (2.25):

$$b_1 = b_2 = -\frac{\ell}{2(\exp(\ell) - 1)} = -\frac{b_3}{2}. \tag{2.26}$$

2.2.2 Perturbation of Ω_n, $n \geq 1$.

We prove that for Λ^{-1} small,

$$\Omega_n(\Lambda) = \Omega_n^{(0)} + \Omega_n^{(1)}\Lambda^{-1} + \mathcal{O}(\Lambda^{-2}), \tag{2.27}$$

where $\Omega_n^{(0)}$ is given by (2.20) and

$$\Omega_n^{(1)} = -\frac{2}{1 + 4\pi^2 n^2 \ell^{-2}}. \tag{2.28}$$

By the implicit function theorem, we may expand the solution of (2.11)–(2.13) and (2.15) as

$$\begin{cases} \kappa_{1,2} = \dfrac{1}{2} \pm \dfrac{in\pi}{\ell} + b_{1,2}\Lambda^{-1} + \mathcal{O}(\Lambda^{-2}), \\ \kappa_3 = 0 + b_3\Lambda^{-1} + \mathcal{O}(\Lambda^{-2}), \\ \Omega_n = \Omega_n^{(0)} + \Omega_n^{(1)}\Lambda^{-1} + \mathcal{O}(\Lambda^{-2}). \end{cases} \tag{2.29}$$

Substituting into (2.11–2.13), we find from the $\mathcal{O}(\Lambda^{-1})$ terms

$$\begin{cases} b_1 + b_2 + b_3 = 0, \\ \Omega_n^{(1)} = -\dfrac{b_1 + b_2}{2} + \dfrac{in\pi}{\ell}(b_1 - b_2) - b_3, \\ b_3 = \left(\dfrac{1}{4} + \dfrac{n^2\pi^2}{\ell^2}\right)^{-1}. \end{cases} \tag{2.30}$$

Substituting into (2.15) we find the leading order term $\mathcal{O}(\Lambda^2)$ vanishes identically; from the next order term $\mathcal{O}(\Lambda)$ we deduce that $b_1 = b_2$. The relation (2.28) follows from this equation and (2.30).

2.3 Spectrum of the Linearized Operator for a Long Fiber

We remind the reader that in this section, Λ and ℓ, without bars, refer to the dimensionless parameters defined by (2.6).

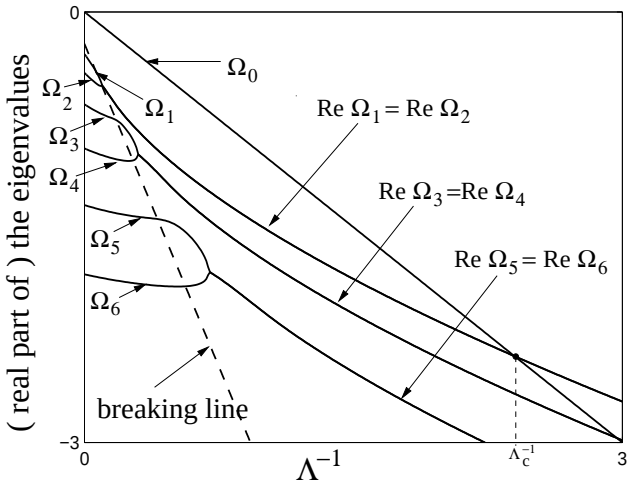

FIGURE 2.1: The evolution of the real parts of the first seven eigenvalues $\Omega_0, \Omega_1, \ldots, \Omega_6$ versus Λ^{-1}, assuming $\ell = 15$. The dashed line is the *breaking line* described in (2.56), the estimate for where the eigenvalues $\Omega_1, \Omega_2, \ldots$ become complex. Λ_c^{-1} is the crossover point such that if $\Lambda^{-1} > \Lambda_c^{-1}$, the eigenvalue which has largest real part, $\Omega_{\max}$, is complex.

To analyze larger values of Λ^{-1}, where the expansion of section 2.2 loses accuracy, we require that $\ell \gg 1$, i.e. we have a long fiber. When Λ^{-1} is small, all eigenvalues are real and ordered by their index: i.e.,

$$\Omega_0 > \Omega_1 > \Omega_2 > \cdots . \tag{2.31}$$

As Λ^{-1} increases, some of the eigenvalues become complex. As this occurs we still retain the ordering

$$\text{Re } \Omega_1 \geq \text{Re } \Omega_2 > \text{Re } \Omega_3 \geq \text{Re } \Omega_4 > \text{Re } \Omega_5 > \cdots . \tag{2.32}$$

However, Ω_0 remains real,[1] and although its position in the sequence (2.32) varies with Λ^{-1}, we retain the index zero. This behavior is illustrated in Figure 2.1, where we have set $\ell = 15$.

2.3.1 Computation of Ω_0

We shall prove that, provided ℓ is sufficiently large, the operator $\mathbf{L}$ has a real eigenvalue

$$\Omega_0 = -\Lambda^{-1} + \mathcal{O}(e^{-\ell}). \tag{2.33}$$

Note that this result is consistent with (2.22). Recall from section 2.2.1 that, in solving (2.11)–(2.13) for small nonzero Λ^{-1}, we found that $\kappa_{1,2}$ became a complex-conjugate pair while κ_3 remained real. Thus for general Λ^{-1} we assume

$$\kappa_{1,2} = \mu \pm i\nu. \tag{2.34}$$

Then (2.11) implies

$$\kappa_3 = 1 - 2\mu. \tag{2.35}$$

[1] This statement breaks down if Λ^{-1} becomes exceedingly large, contradicting our implicit assumption that $\Lambda^{-1} \ll \ell$.

We use (2.12)–(2.14) to solve for μ, ν, and Ω as follows. Dividing the middle row of (2.14) by $e^{\kappa_3 \ell}$, we rewrite this equation as

$$\det \begin{pmatrix} \kappa_1 & \kappa_2 & \kappa_3 \\ \kappa_1 e^{(\kappa_1-\kappa_3)\ell} & \kappa_2 e^{(\kappa_2-\kappa_3)\ell} & \kappa_3 \\ \Omega_0 - \kappa_1^2 & \Omega_0 - \kappa_2^2 & \Omega_0 - \kappa_3^2 \end{pmatrix} = 0. \tag{2.36}$$

Now provided

$$\mu < \frac{1}{3}, \tag{2.37}$$

we have for the 2,1- and 2,2-entries of this determinant

$$|e^{(\kappa_j-\kappa_3)\ell}| = e^{-(1-3\mu)\ell} \ll 1, \tag{2.38}$$

since $\ell \gg 1$. Thus neglecting these entries and recalling (2.34)–(2.35), we conclude

$$\Omega_0 = -(\mu^2 + \nu^2) + \mathcal{O}(e^{-(1-3\mu)\ell}). \tag{2.39}$$

On the other hand, we substitute (2.34)–(2.35) into (2.12) to find

$$\Omega_0 = -(\mu^2 + \nu^2) - 2\mu(1 - 2\mu). \tag{2.40}$$

Comparing (2.39) and (2.40), we deduce

$$\mu(1 - 2\mu) = \mathcal{O}(e^{-(1-3\mu)\ell}). \tag{2.41}$$

By (2.37), we have $1 - 2\mu > 1/3 > 0$, so dividing (2.41) by $1 - 2\mu$, we obtain

$$\mu = \mathcal{O}(e^{-(1-3\mu)\ell}). \tag{2.42}$$

Thus assumption (2.37) is consistent and, moreover,

$$\mu = \mathcal{O}(e^{-(1-3\mu)\ell}) = \mathcal{O}(e^{-\ell}). \tag{2.43}$$

Returning to (2.39), we conclude that

$$\Omega_0 = -\nu^2 + \mathcal{O}(e^{-\ell}). \tag{2.44}$$

But substituting (2.34)–(2.35) into (2.13) and working with (2.43), we see

$$\Lambda^{-1} = \nu^2 + \mathcal{O}(e^{-\ell}). \tag{2.45}$$

The claim (2.33) follows on eliminating ν from (2.44)–(2.45).

As one might expect with an exponentially small error, (2.33) agrees extremely well with the numerical results. Indeed the graph of (2.33) cannot be distinguished visually from the graph of Ω_0 in Figure 2.1.

Incidentally, the eigenfunction associated with Ω_0 exhibits unusual behavior for a one-dimensional eigenvalue problem—the number of its zeros or nodes changes as Λ^{-1} varies. Specifically, modulo terms that are exponentially small (outside of a boundary layer near $x = \ell$), the nondimensionalized eigenfunction is just $\cos(x/\sqrt{\Lambda})$.

2.3.2 Later eigenvalues, real case

In this subsection, we characterize a range of Λ^{-1}, as this parameter increases from 0, in which the eigenvalue Ω_n is real. Continuing the structure of the roots κ_j inherited from small Λ^{-1}, we assume

$$\kappa_{1,2} = \mu \pm i\nu \tag{2.46}$$

and invoke (2.11) to conclude

$$\kappa_3 = 1 - 2\mu. \tag{2.47}$$

We shall solve (2.15) for ν and substitute the result into (2.12)–(2.13) to obtain a parametric representation of the curve $\Omega = \Omega_n(\Lambda^{-1})$ in the Λ^{-1}, Ω-plane, with μ as the parameter. (It is not practical to solve explicitly for Ω_n as a function of Λ^{-1}.)

Let us divide the second row of the determinant (2.15) by $\exp(\mu\ell)$, obtaining

$$\det \begin{pmatrix} 1 & 1 & 1 \\ e^{i\nu\ell} & e^{-i\nu\ell} & e^{(1-3\mu)\ell} \\ \kappa_1^{-2} & \kappa_2^{-2} & \kappa_3^{-2} \end{pmatrix} = 0. \tag{2.48}$$

If

$$\mu > \frac{1}{3}, \tag{2.49}$$

then for large ℓ we may neglect the $2,3$-entry of this determinant, so that the equation reduces to

$$e^{2i\nu\ell} = \frac{\kappa_2^2(\kappa_1^2 - \kappa_3^2)}{\kappa_1^2(\kappa_2^2 - \kappa_3^2)} + \mathcal{O}(e^{-(3\mu-1)\ell}). \tag{2.50}$$

Equation (2.50) suggests that $\nu\ell = \mathcal{O}(1)$ or

$$\nu = \mathcal{O}(\ell^{-1}). \tag{2.51}$$

Assuming this and recalling (2.49), we see that the right-hand side of (2.50) equals $1 + \mathcal{O}(\ell^{-1})$. Solving (2.50), we find

$$\nu = n\pi \cdot \ell^{-1} + \mathcal{O}(\ell^{-2}), \qquad n = 1, 2, \ldots, \tag{2.52}$$

confirming our assumption (2.51). On the other hand, substituting (2.46)–(2.47) into (2.11)–(2.12), we find

$$\begin{cases} \Lambda^{-1} = (1 - 2\mu)(\mu^2 + \nu^2), \\ \Omega_n = 3\mu^2 - 2\mu - \nu^2. \end{cases} \tag{2.53}$$

Substituting (2.52) into (2.53), we obtain the parametric representation

$$\begin{cases} \Lambda^{-1} = (1 - 2\mu) \cdot (\mu^2 + n^2\pi^2\ell^{-2}) + \mathcal{O}(\ell^{-3}), \\ \Omega_n = 3\mu^2 - 2\mu - n^2\pi^2\ell^{-2} + \mathcal{O}(\ell^{-3}). \end{cases} \tag{2.54}$$

Note from (2.54) that $\Lambda^{-1} = 0$ occurs when $\mu = 1/2$. (This may also be seen by solving (2.11)–(2.14) directly when $\Lambda^{-1} = 0$, which avoids the $\mathcal{O}(\ell^{-3})$ error in (2.54).) Recalling (2.49), we conclude that

$$1/3 < \mu \leq 1/2 \tag{2.55}$$

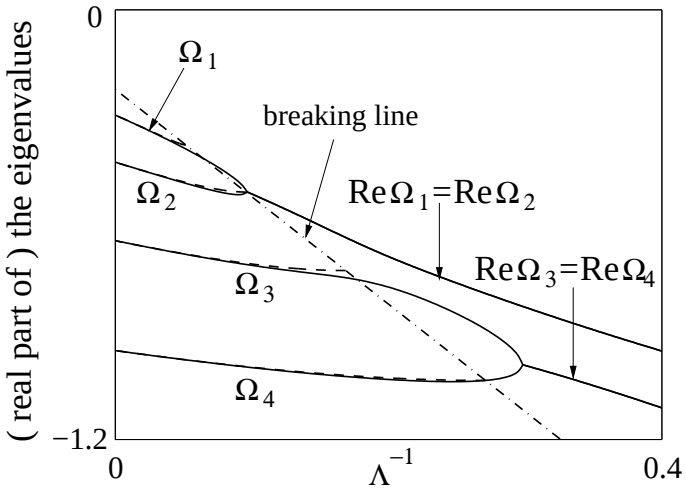

FIGURE 2.2: A comparison between the computations (solid lines) and the theoretical approximations given by (2.54) (dashed lines) of the eigenvalues $\Omega_1, \ldots, \Omega_4$ while they are real. The approximation terminate at the breaking line, given by (2.56). The dimensionless cable length ℓ is 15.

is the relevant parameter range in (2.54). At the lower end of the range, the points (Λ^{-1}, Ω) in (2.54) all lie along the line

$$\Omega = -3\Lambda^{-1} - 2/9, \tag{2.56}$$

which we call the *breaking line*. This may be seen, neglecting the $\mathcal{O}(\ell^{-3})$-errors, by setting $\mu = 1/3$ in (2.53) and eliminating ν^2.

The approximations (2.54), for $n = 1, 2, 3, 4$ and for μ satisfying (2.55), are graphed in Figure 2.2, along with the computed eigenvalues. As the figure emphasizes, the asymptotics underlying (2.54) break down as $\mu \to 1/3$. More precisely, for μ near $1/3$, exceedingly large values of ℓ are needed to make (2.54) accurate, and increasingly so as n becomes large.

Incidentally, note that for $\Lambda^{-1} = 0$,

$$\frac{d\,\Omega_n}{d\Lambda^{-1}} = \frac{d\,\Omega_n/d\mu}{d\Lambda^{-1}/d\mu}\Big|_{\mu=\frac{1}{2}} = -\frac{2}{1 + 4n^2\pi^2\ell^{-2}}, \tag{2.57}$$

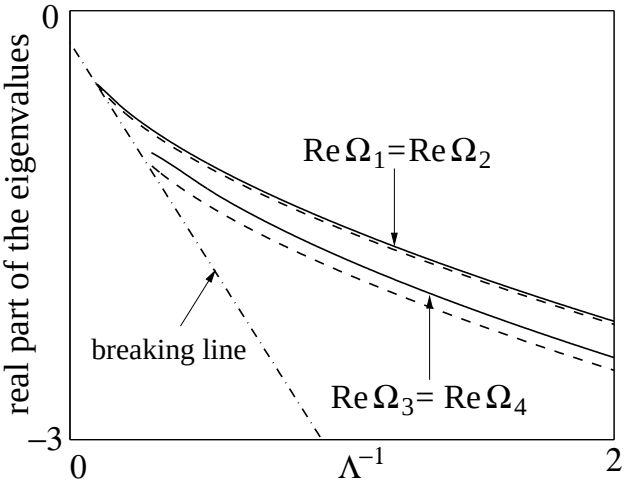

FIGURE 2.3: A comparison between the computations (solid lines) and the theoretical approximations given by (2.66), (2.70) (dashed lines) of the real parts of the eigenvalues $\Omega_1, \ldots, \Omega_4$ while they are complex. The dimensionless cable length ℓ is 15.

which is consistent with (2.28), even without the $\mathcal{O}(\ell^{-3})$-errors in (2.54).

2.3.3 Later eigenvalues, complex case

Motivated by the numerical results, when the above asymptotics break down we look for complex eigenvalues. Let us define

$$\mu = \frac{1}{2}\,\mathrm{Re}\,(\kappa_1 + \kappa_2), \tag{2.58}$$

$$\nu = \frac{1}{2}\,\mathrm{Im}\,(\kappa_1 + \kappa_2). \tag{2.59}$$

Then

$$\kappa_{1,2} = \mu + i\nu \pm \delta, \tag{2.60}$$

where δ, possibly complex, is to be determined, and (2.11) implies that

$$\kappa_3 = 1 - 2(\mu + i\nu). \tag{2.61}$$

Even in the complex case, we continue to assume (2.49). Thus, asymptotically for large ℓ, the determinant equation (2.15) may be simplified to

$$e^{2\,\delta\ell} = \frac{\kappa_2^2(\kappa_1^2 - \kappa_3^2)}{\kappa_1^2(\kappa_2^2 - \kappa_3^2)} + \mathcal{O}(e^{-(3\mu-1)\ell}). \tag{2.62}$$

As above, we solve (2.62) to obtain

$$\delta = in\pi \cdot \ell^{-1} + \mathcal{O}(\ell^{-2}), \quad n = 1, 2, \ldots. \tag{2.63}$$

We determine the real parameter ν from the condition that Λ^{-1} must be real: i.e., by equation (2.13)

$$\text{Im } (\kappa_1\kappa_2\kappa_3) = 0, \tag{2.64}$$

and from this we deduce that

$$\nu = \pm\Big\{\mu(3\mu - 1) + n^2\pi^2\ell^{-2} + \mathcal{O}(\ell^{-3})\Big\}^{1/2}. \tag{2.65}$$

Substituting into (2.12)–(2.13), we obtain a parametric representation of Ω versus Λ^{-1}. Specifically, adjusting indices to account for the fact that (2.65) has two solutions, we find

$$\Lambda^{-1} = \mu(4\mu - 1)^2 + 4\mu \cdot n^2\pi^2\ell^{-2} + \mathcal{O}(\ell^{-3}), \tag{2.66}$$

$$\Omega_{2n} = (\mu + i\nu)(3\mu + 3i\nu - 2) - n^2\pi^2\ell^{-2} + \mathcal{O}(\ell^{-3}), \tag{2.67}$$

$$\Omega_{2n-1} = \overline{\Omega}_{2n}, \tag{2.68}$$

where ν is given by (2.65) and

$$1/3 < \mu < \infty. \tag{2.69}$$

By substituting $\mu = 1/3$ into (2.66), (2.67) we see that these approximations terminate at the breaking line (2.56). Several of them are graphed in Figure 2.3, along with

the computed eigenvalues. Incidentally, note that the real parts of the eigenvalues may be written more simply, without ν:

$$\text{Re } \Omega_{2n-1} = \text{Re } \Omega_{2n} = -\mu(6\mu - 1) - 4n^2\pi^2\ell^{-2} + \mathcal{O}(\ell^{-3}). \tag{2.70}$$

To explore the transition between the real and complex cases, we substitute the limiting value $\mu = 1/3$ into (2.54) and (2.66), (2.67). For the even-index eigenvalues, both the real and complex cases give same result,

$$\Lambda^{-1} = \frac{1}{27} + \frac{1}{3}\left(\frac{2n\pi}{\ell}\right)^2 + \mathcal{O}(\ell^{-3}), \tag{2.71}$$

$$\Omega_{2n} = -\frac{1}{3} - \left(\frac{2n\pi}{\ell}\right)^2 + \mathcal{O}(\ell^{-3}), \tag{2.72}$$

which of course lies on the breaking line (2.56). For odd-index eigenvalues, there is an $\mathcal{O}(\ell^{-2})$ jump between the results of substituting $\mu = 1/3$ into (2.54) and into (2.66), (2.67). Hints of this behavior may be seen in Figure 2.2—the asymptotic approximation of Ω_{2n} in the real case continues to be defined closer to the actual transition to complex eigenvalues than that of Ω_{2n-1}. Incidentally, (2.71) may be used to estimate the largest value of Λ^{-1} at which Ω_{2n-1} and Ω_{2n} are still real.

Let us relate these formulae to a result of Echebarria and Karma [12]. Invoking considerations of group velocity and bifurcation theory, those authors argue that, at the onset of instability, the complex wave number ($\kappa = \mu + i\nu$ in our notation) ought to satisfy

$$2\kappa^3 - \kappa^2 + \frac{1}{\Lambda} = 0. \tag{2.73}$$

(This relation is equivalent to their equation (56) written in our notation.) Now to leading order (2.65), (2.66) assert that

$$\nu^2 = \mu(3\mu - 1), \quad 16\mu^3 - 8\mu^2 + \mu = \Lambda^{-1}. \tag{2.74}$$

It may be checked that these two real equations are equivalent to the single complex equation (2.73). Thus we have given an independent derivation of (2.73) that does not rely on computing group velocities for waves that grow exponentially in space and that accounts explicitly for boundary conditions on a (long) finite-length cable.

2.4 Summary

Let us summarize the asymptotic results from section 2.3 regarding the eigenvalues of the linear operator of (2.3), which is $\bar{w}^2\mathbf{L} = (w^2/\xi^2)\cdot\mathbf{L}$. For this task, and for the remainder of this Chapter, we shall undo the scaling (2.6) and return to the dimensional parameters. We found the following:

- Ω_0 is always real, given by

$$\Omega_0 = -\frac{\xi^2}{w\Lambda} + \mathcal{O}(e^{-w\ell/\xi^2}). \tag{2.75}$$

- For $n \geq 1$, Ω_n is real if Λ^{-1} is below a threshold. Equation (2.71) estimates that the threshold for Ω_{2n-1} and Ω_{2n} to become complex is

$$\frac{w^3}{27\xi^4} + \frac{w}{3}\left(\frac{2n\pi}{\ell}\right)^2 + \mathcal{O}(\ell^{-3}). \tag{2.76}$$

- In the real case, the relation between Λ^{-1} and Ω_n is given parametrically by

$$\begin{cases} \Lambda^{-1} = \xi^{-2}(w - 2\mu\xi)\cdot(\mu^2 + n^2\pi^2\xi^2\ell^{-2}) + \mathcal{O}(\ell^{-3}), \\ \Omega_n = 3\mu^2 - 2\mu w/\xi - n^2\pi^2\xi^2\ell^{-2} + \mathcal{O}(\ell^{-3}), \end{cases} \tag{2.77}$$

  where $w/3\xi < \mu \leq w/2\xi$.

- In the complex case, the relation between Λ^{-1} and the real parts of Ω_{2n-1}, Ω_{2n}

is given parametrically by

$$\begin{cases} \Lambda^{-1} = \mu\xi^{-1}(4\mu - w/\xi)^2 + 4\mu\xi \cdot n^2\pi^2\ell^{-2} + \mathcal{O}(\ell^{-3}), \\ \text{Re } \Omega_{2n-1} = \text{Re } \Omega_{2n} = -\mu(6\mu - w/\xi) - 4n^2\pi^2\xi^2\ell^{-2} + \mathcal{O}(\ell^{-3}), \\ \text{Im } \Omega_{2n-1} = -\text{Im } \Omega_{2n} = 2(3\mu - w/\xi)\Big[\mu(3\mu - w/\xi) + n^2\pi^2\xi^2\ell^{-2}\Big]^{1/2} + \mathcal{O}(\ell^{-3}), \end{cases} \tag{2.78}$$

where $w/3\xi < \mu < \infty$.

Consider bifurcation of (2.1) from the zero solution as σ increases. An eigenvalue of the linearization crosses into the (unstable) right-half plane when $\sigma = \text{Re } \Omega_{\max}$, where $\Omega_{\max}$ is the eigenvalue of (2.3) with the (algebraically) largest real part. If Λ^{-1} is small, Ω_0 is the largest eigenvalue, its associated eigenfunction is real, and a time-independent stationary-wave solution of (2.1) appears at the bifurcation. However, Ω_0 decreases more rapidly with Λ^{-1} than later eigenvalues, which, moreover, become complex. Thus, when Λ^{-1} is sufficiently large, say $\Lambda^{-1} > \Lambda_c^{-1}$, $\Omega_{\max}$ will be complex, and time-oscillatory travelling-wave solutions will appear at the bifurcation (see [12] for more details). To estimate the crossover value Λ_c^{-1}, we consider the equation $\Omega_0 = \text{Re } \Omega_1$. Recalling (2.75), we may rewrite this equation to leading order as

$$-\frac{\xi^2}{w\Lambda} = \text{Re } \Omega_1. \tag{2.79}$$

Substituting the first and second equations of (2.78) into the left and right sides of (2.79), respectively, we obtain the quadratic equation

$$8\mu^2 - 7(w/\xi) \cdot \mu + (w/\xi)^2 = 0$$

for the value of μ associated with the crossover. We select the root $\mu = (7 + \sqrt{17})w/16\xi$ that satisfies $\mu > w/3$ and substitute into (2.66) to obtain the leading order estimate

$$\Lambda_c^{-1} \approx \frac{71 + 17\sqrt{17}}{64} \cdot \frac{w^3}{\xi^4}. \tag{2.80}$$

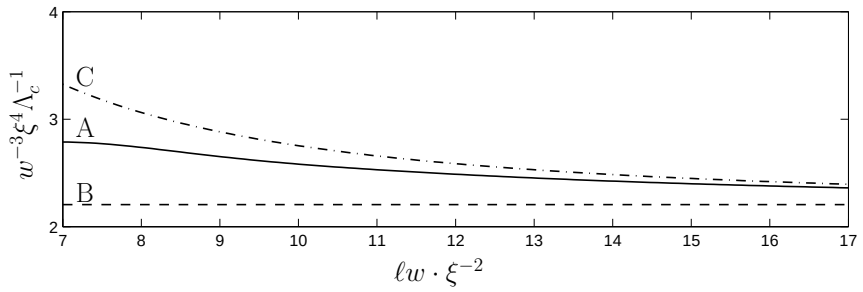

FIGURE 2.4: A comparison among the computational result (curve A) for Λ_c^{-1}, the theoretical leading order approximation (2.80) (line B), and the second order approximation (2.81) (curve C). The x-axis is the cable length ℓ scaled by $w\xi^{-2}$, and y-axis is the critical value Λ_c^{-1} scaled by $w^{-3}\xi^4$. With these scalings, the curves are independent of ξ and w.

By carrying $\mathcal{O}(\ell^{-2})$ terms in the above calculation, one may extend this estimate to next order,

$$\Lambda_c^{-1} = \frac{w^3}{\xi^4}\left\{\frac{71+17\sqrt{17}}{64} + \frac{(7+\sqrt{17})\pi^2}{2}\cdot\left(\frac{w\ell}{\xi^2}\right)^{-2}\right\} + \mathcal{O}(\ell^{-3}). \tag{2.81}$$

Figure 2.4 shows a comparison between the computational result for Λ_c^{-1} and theoretical approximations (2.80) and (2.81) for various (large) cable lengths ℓ. Observe that the computational value is between the values of (2.80) and (2.81). For ℓ smaller than shown in the figure, the graph of Λ_c^{-1} changes character. A hint of such behavior may be gleaned from the fact that the approximation (2.81) blows up as ℓ^{-2} when ℓ tends to zero. We plan to investigate these phenomena more thoroughly in the future.

Table 2.1 summarizes the results of two simulations that illustrate the different behavior that occurs for $\Lambda^{-1} > \Lambda_c^{-1}$ and $\Lambda^{-1} < \Lambda_c^{-1}$. By contrast, the simulation shown in Figure 2.5 were performed on a cable of length 25 cm, which corresponds to a scaled, dimensionless length

$$\bar{\ell} = w\ell/\xi^2 = 8.84. \tag{2.82}$$

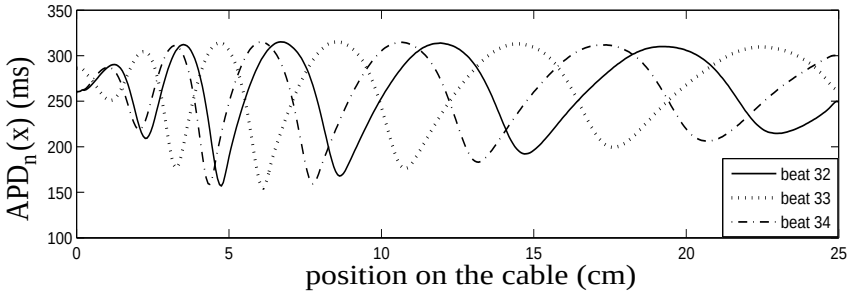

FIGURE 2.5: Simulation of the cable equation for the two-current model (1.19) with parameters given in the Table 1.2, assuming a periodic stimulus with basic cycle length 343ms. The x-axis is the position on the cable, the y-axis is $A_n(x)$ for the values of n listed above. As predicted by using (2.81), the pattern is propagating.

For this length, the (dimensionless) critical value Λ_c^{-1}(computed numerically — curve A in Figure 2.4) equals 2.67, which in dimensional units gives the value listed in Table 2.1. Since $\Lambda^{-1} > \Lambda_c^{-1}$, the modulation equation predicts that alternans will appear in travelling patterns. The behavior is observed in the simulation of Figure 2.5, which shows $A_n(x)$ for several beats about halfway through the transient to steady state. The simulation of Noble's model in Figure 1.7 shows a pattern of standing wave, where $\Lambda^{-1} < \Lambda_c^{-1}$. The key behavior relevant here is that the conduction-velocity curve is exceptionally flat at the critical diastolic interval, which makes $\Lambda^{-1} = 2c'/c^2$ small.

Table 2.1: Results of two simulations: two-current model and Noble's model. w, ξ, ℓ have units of length in cm; Λ^{-1} and Λ_c^{-1} have units of inverse length in cm^{-1}.

Name of model	w	ξ	ℓ	Λ^{-1}	Λ_c^{-1}	Observed alternans
Two-current	0.034	0.310	25	0.206	0.011	Traveling
Noble	0.045	0.180	20	0.020	0.198	Stationary

3

Bifurcations in the Modulation Equation

In this chapter, we continue our bifurcation analysis on the Echebarria-Karma modulation equation (2.1).

As we have seen in Chapter 2, the trivial steady state solution $a \equiv 0$ of (2.1) loses its stability as σ increases. We analyzed the eigenvalues of the linear operator that maps a function $a(x)$ to (2.3) subject to Neumann boundary conditions, and we concluded that the first bifurcation we observe as σ increases may be steady state bifurcation if $\Lambda^{-1} < \Lambda_c^{-1}$ or Hopf bifurcation otherwise, where the critical value Λ_c^{-1} depends on ℓ, w and ξ. In this chapter, extending our previous result, we simulate and analyze the bifurcation of (2.1) when Λ^{-1} is close to Λ_c^{-1} and hence competition between multiple modes appears.

Recall that in Chapter 2, we define dimensionless variables in (2.6), then the operator in (2.3) can be written as $w^2\xi^{-2}\cdot\mathbf{L}a$, where $\mathbf{L}$ is given in (2.7). For convenience in this Chapter we will omit all the bars in (2.7). The no-flux (Neumann) boundary conditions are given in (2.2).

Obviously $a(x,t) \equiv 0$ is a trivial solution to (2.1). When σ is small (including all negative values), the zero solution is linearly stable. As σ increases to beyond some

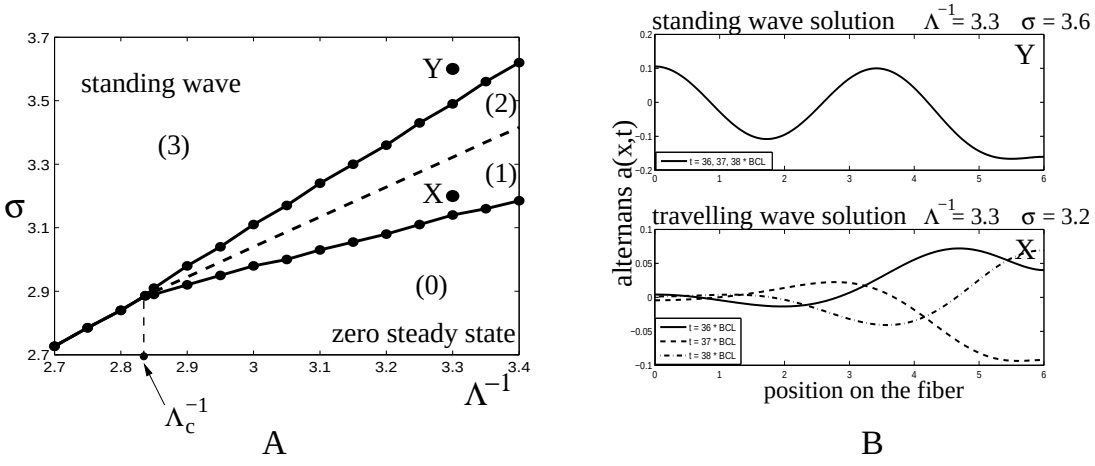

FIGURE 3.1: **A**: The bifurcation diagram for Λ^{-1} near Λ_c^{-1} when $\ell = 6$. There are four regions each denoting different behavior of the solution: (0), trivial zero steady state solution, (1), pure periodic solution, (2), mixed-mode periodic solution and (3) standing wave solution. **B**: Two simulated solutions whose parameters correspond to X and Y in Figure 3.1A. The upper one is a standing wave and the lower one has a travelling pattern

threshold, the zero solution loses its stability. This bifurcation at $\sigma = -\text{Re }\Omega_{\max}$ can be either steady state or Hopf, depending on whether $\Omega_{\max}$ is real or complex. In Chapter 2 we showed that for fixed fiber length ℓ, there is a critical value Λ_c^{-1} such that whether $\Omega_{\max}$ is real or complex is determined by whether Λ^{-1} is less or greater than Λ_c^{-1}. In the critical case, i.e. when $\Lambda^{-1} = \Lambda_c^{-1}$, we have $\Omega_0 = \text{Re }\Omega_{1,2}$ and both Hopf and steady state modes become unstable simultaneously.

3.1 Competition between Modes Near the Critical Point

In this Chapter we fix the dimensionless length of the cardiac fiber to be $\ell = 6$ to illustrate the dynamics. The evolution of the eigenvalues of the linear operator $\mathbf{L}$ has a similar behavior as in Figure 2.1, in which ℓ was assumed to be a large value 15. We use $\ell = 6$ as an example to illustrate that the analysis we are going to perform does not require ℓ to be large. We find by computation that for $\ell = 6$, the critical point $\Lambda_c^{-1} \approx 2.837$.

Figure 3.1A illustrates the simulation results of the dynamics of the solution to the modulation equation (2.1) when Λ^{-1} is near the critical value Λ_c^{-1}. If (Λ^{-1}, σ) lies in the region (3) in Figure 3.1A, the stable solution of (2.1) is a steady pattern; for example the solution corresponding to point Y in Figure 3.1A is illustrated in Figure 3.1B (upper). If $\Lambda^{-1} < \Lambda_c^{-1}$ is fixed and σ crosses into region (3), this steady solution appears through a single, simple bifurcation as discussed in Chapter2. However if $\Lambda^{-1} > \Lambda_c^{-1}$ is fixed and σ is increased, the situation is more complicated. The first bifurcation is to a periodic solution; for example, the solution corresponding to point X in Figure 3.1A is illustrated in Figure 3.1B (lower). However, as σ is increased further, the solution evolves to a steady pattern through two secondary bifurcations.

To better understand this behavior, consider the solution as a function of time at a fixed point x_o. For $x_o = \frac{15}{20} \times \ell = 4.5$ and $\Lambda^{-1} = 3.3$ (note that $\Lambda^{-1} > \Lambda_c^{-1}$), Figure 3.2 shows how the quantity

$$\max_t a(x_o, t) - \min_t a(x_o, t) \tag{3.1}$$

(dashed line) and the average

$$\frac{1}{T} \int_0^T a(x_o, t)\, dt, \tag{3.2}$$

where T is the period (solid line), vary with σ for $3 < \sigma < 3.7$. In region (1), which we call the pure-periodic region, the average of the solution is close to zero. By contrast, in region (2), although the solution continues to oscillate, its average is nonzero. Finally, in region (3) the solution is steady (and equal to its average).

In the following sections we provide supporting theory for the above observation. In particular we shall see that the transitions between region (1) and (2) and between (2) and (3) represent secondary bifurcations that appear from unfolding the degenerate bifurcation for $\Lambda^{-1} = \Lambda_c^{-1}$.

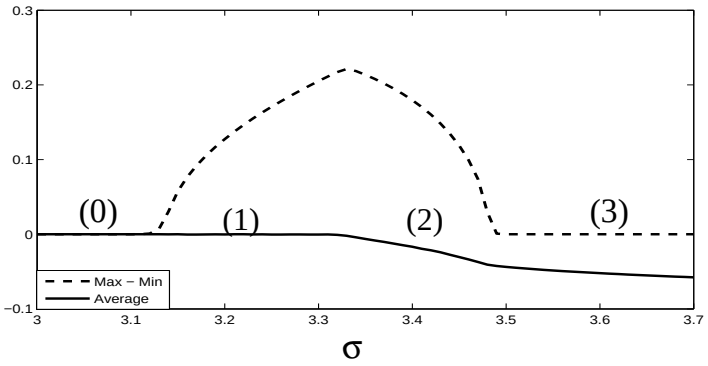

FIGURE 3.2: The simulation result for the oscillation amplitude, $\max_t a(x_o,t) - \min_t a(x_o,t)$ (dashed curve), and the average of $a(x_o,t)$ (solid curve) in one period for various values of σ when $\Lambda^{-1} = 3.3$ and $x_o = 4.5$. The four labels refer to regions in Figure 3.1A: (0) for $\sigma < 3.14$, zero steady state solution, both amplitude and average are zero, (1) for $3.14 < \sigma < 3.32$, pure periodic solution, the amplitude is nonzero but the average is zero (to leading order), (2) for $3.32 < \sigma < 3.49$, mixed mode solution, both amplitude and average are nonzero, (3) for $\sigma > 3.49$, standing wave, with no oscillation and nonzero average.

3.2 Reduction to a Three Dimensional System

We consider the case when the parameter Λ^{-1} exactly equals to the critical value Λ_c^{-1}, so we have

$$\Omega_0 = \text{Re } \Omega_{1,2} > \text{Re } \Omega_{3,4} > \ldots,$$

which are all negative. For appropriate σ, we apply center-manifold theory [7, 24] to show that the dynamics of the solution to (2.1) is determined by the first three modes corresponding to $\Omega_{0,1,2}$.

First we rewrite the modulation equation (2.1) in a more convenient way. Define $\tilde{\sigma} = \sigma - \sigma_c$, the increment of σ away from its bifurcation value $\sigma_c = -\Omega_0$. In dimensionless variables, (2.1) can be rewritten as

$$\partial_t a = \tilde{\sigma} a + \mathscr{L}\, a - a^3, \tag{3.3}$$

where

$$\mathscr{L}\, a = \sigma_c a + a'' - a' - \Lambda_c^{-1} \int_0^x a(x')dx' \tag{3.4}$$

and we have assumed the positive nonlinear coefficient $g = 1$ by a scaling $a \to g^{-1/2} \cdot a$.

The eigenvalues of $\mathscr{L}$ are $\widetilde{\Omega}_n = \Omega_n + \sigma_c = \Omega_n - \Omega_0$ for $n = 0, 1, 2, \ldots$. Thus the first three eigenvalues are all on the imaginary axis:

$$\widetilde{\Omega}_0 = 0,\ \widetilde{\Omega}_{1,2} = \pm \mathbf{i}\, \omega, \tag{3.5}$$

where $\omega > 0$ is real. All other eigenvalues are in the left half plane. Let $\phi_0(x)$ be the eigenfunction with eigenvalue $\widetilde{\Omega}_0$ and $\phi_1(x) \pm \mathbf{i}\, \phi_2(x)$ be the eigenfunctions with eigenvlaues $\widetilde{\Omega}_{1,2}$, i.e.

$$\mathscr{L}\phi_0 = 0 \quad \text{and} \quad \mathscr{L}(\phi_1 \pm \mathbf{i}\, \phi_2) = \pm \mathbf{i}\, \omega(\phi_1 \pm \mathbf{i}\, \phi_2), \tag{3.6}$$

where ϕ_0, ϕ_1, ϕ_2 are all real. Let $E^c = \text{span}\{\phi_0, \phi_1, \phi_2\}$, i.e. E^c is the central subspace. We study the dynamics of $a(x,t)$ through its projection onto the central subspace.

We regard the solution to (3.3) as a flow in the function space of L^2 on the interval $(0, \ell)$, i.e. square integrable functions. By the central manifold theorem [7, 24], there exists a central manifold $\mathcal{M}$ which is invariant under the flow and tangent to the central space E^c, and there is also a neighborhood of zero in L^2, denoted by U, with the following property: if $a(\cdot, t)$ is a solution of (3.3) such that for all $t > 0$, $a(\cdot, t) \in U$, then the distance from $a(\cdot, t)$ to $\mathcal{M}$ converges to zero exponentially. In other words, to understand the long-time dynamics of (3.3) near 0, it is sufficient to examine the flow on $\mathcal{M}$. The flow on $\mathcal{M}$ is a three dimensional ODE, which can be formulated by using the coordinates of E^c .

We first introduce the adjoint operator of $\mathscr{L}$, which is defined as below:

$$\mathscr{L}^* a = \sigma_c a + a'' + a' - \Lambda_c^{-1} \int_x^\ell a(x')dx', \tag{3.7}$$

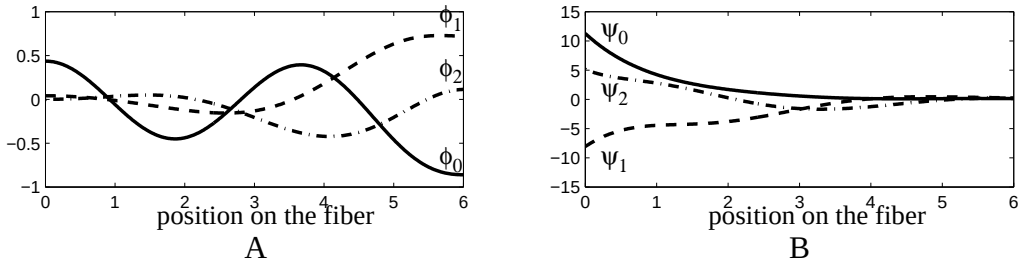

FIGURE 3.3: Illustration of the eigenfunctions $\phi_{0,1,2}$ in (3.6) and $\psi_{0,1,2}$ in (3.9) , assuming the length of the fiber $\ell = 6$. They satisfy the conditions of orthogonality (3.10).

with boundary conditions

$$a'(0) + a(0) = a'(\ell) + a(\ell) = 0. \tag{3.8}$$

The adjoint operator $\mathscr{L}^*$ has the same eigenvalues as $\mathscr{L}$. Let ψ_0, $\psi_1 \pm \mathbf{i}\,\psi_2$ be the first three eigenfunctions of $\mathscr{L}^*$, i.e.,

$$\mathscr{L}^*\psi_0 = 0 \quad \text{and} \quad \mathscr{L}^*(\psi_1 \pm \mathbf{i}\,\psi_2) = \mp \mathbf{i}\,\omega \cdot (\psi_1 \pm \mathbf{i}\,\psi_2), \tag{3.9}$$

where ψ_0, ψ_1 and ψ_2 are all real.We may impose the following conditions of orthogonality:

$$\langle \psi_i, \phi_j \rangle = \delta_{ij}, \quad \text{for } \; i, j = 0, 1, 2, \tag{3.10}$$

where the inner product $\langle , \rangle$ is taken in the L^2–sense. Figure 3.3 shows a possible choice of $\phi_i(x)$ and $\psi_i(x)$ for $i = 0, 1, 2$.

We now parameterize $\mathcal{M}$ by E^c. Let $\mathcal{H} = \{\psi_0, \psi_1, \psi_2\}^\perp$; then $\mathcal{H}$ is a complement of E^c in L^2, i.e. $L^2 \cong E^c \oplus \mathcal{H}$. Let π be the projection onto E^c with kernel $\mathcal{H}$. Since $\mathcal{M}$ is tangent to E^c, for all $u = \sum_{i=0}^{2} u_i \phi_i$ in $E^c \cap U$, there is a unique $J(u) \in \mathcal{M}$ such that $\pi J(u) = u$. Moreover, the difference $R(u) = J(u) - u$ belongs to $\mathcal{H}$ and satisfies

$$R(u) = \mathcal{O}(|u|^2). \tag{3.11}$$

Suppose $a(x,t)$ is a solution of (3.3) such that for all time $a(\cdot,t) \in \mathcal{M} \cap U$. Let $u(t) = \pi a(\cdot,t)$. Of course $a(\cdot,t) = J(u(t))$. To derive an ODE for $u(t)$, we calculate

$$\begin{aligned} \dot{u} = \pi \dot{a} &= \tilde{\sigma} u + \pi \mathscr{L} J(u) - \pi[J(u)^3] \\ &= \tilde{\sigma} u + \pi \mathscr{L} u + \pi \mathscr{L} R(u) - \pi(u^3 + \mathcal{O}(|u|^4)). \end{aligned} \tag{3.12}$$

Clearly $\pi \mathscr{L} u = \mathscr{L} u$ for $\mathscr{L} u \in E^c$ since $u \in E^c$. Since $R(u) \in \mathcal{H}$, for $j = 0, 1, 2$, we have $\langle \psi_j, \mathscr{L} R(u) \rangle = \langle \mathscr{L}^* \psi_j, R(u) \rangle = 0$, i.e. $\mathscr{L} R(u) \in \mathcal{H}$ and hence $\pi \mathscr{L} R(u) = 0$. Thus (3.12) can be rewritten as

$$\dot{u} = \tilde{\sigma} u + \mathscr{L} u - \pi(u^3) + \mathcal{O}(|u|^4). \tag{3.13}$$

Let us regard E^c, a subspace of L^2, as a three-dimensional vector space with coordinates (u_0, u_1, u_2) defined by

$$u = \sum_{i=0}^{2} u_i(t) \phi_i(x).$$

To expand (3.13) in coordinates, we take the inner product of this equation with each ψ_j for $j = 0, 1, 2$. Since $u^3 - \pi(u^3) \in \mathcal{H} = \{\psi_0, \psi_1, \psi_2\}^\perp$, we conclude that $\langle \psi_j, \pi(u^3) \rangle = \langle \psi_j, u^3 \rangle$ for $j = 0, 1, 2$. By (3.6) and (3.10), we obtain the ODE system for each coordinate $u_i(t)$:

$$\begin{cases} \dot{u}_0 = \tilde{\sigma} u_0 - \langle \psi_0, (\sum_{i=0}^{2} u_i \phi_i)^3 \rangle + \mathcal{O}(|u|^4), \\ \dot{u}_1 = \tilde{\sigma} u_1 - \omega u_2 - \langle \psi_1, (\sum_{i=0}^{2} u_i \phi_i)^3 \rangle + \mathcal{O}(|u|^4), \\ \dot{u}_2 = \tilde{\sigma} u_2 + \omega u_1 - \langle \psi_2, (\sum_{i=0}^{2} u_i \phi_i)^3 \rangle + \mathcal{O}(|u|^4). \end{cases} \tag{3.14}$$

We expand $(\sum_{i=0}^{2} u_i \phi_i)^3$ in each equation in (3.14), and the coefficient for each term $u_0^{i_0} u_1^{i_1} u_2^{i_2}$, where $i_0 + i_1 + i_2 = 3$, in the j-th equation is given by

$$h^j_{i_0 i_1 i_2} = \langle \psi_j, \phi_0^{i_0} \phi_1^{i_2} \phi_0^{i_3} \rangle = \int_0^\ell \psi_j \phi_0^{i_0} \phi_1^{i_2} \phi_0^{i_3} \, dx. \tag{3.15}$$

Table 3.1: The value of the coefficients $h^j_{i_0 i_1 i_2}$ in system (3.16).

(i_0, i_1, i_2)	$3,0,0$	$2,1,0$	$2,0,1$	$1,2,0$	$1,1,1$	$1,0,2$	$0,3,0$	$0,2,1$	$0,1,2$	$0,0,3$
$h^0_{i_0 i_1 i_2}$	0.168	−0.070	−0.346	0.081	0.010	0.582	0.004	−0.053	−0.021	−0.084
$h^1_{i_0 i_1 i_2}$	0.008	0.132	−0.152	−0.104	0.021	0.160	0.107	−0.228	0.262	−0.040
$h^2_{i_0 i_1 i_2}$	0.055	−0.024	−0.188	0.012	0.017	0.146	−0.015	0.023	0.012	0.096

For instance, $h^1_{2,1,0} = \langle \psi_1, \phi_0^2 \phi_1 \rangle = \int_0^\ell \psi_1 \phi_0^2 \phi_1 \, dx$. Choosing the functions ϕ_i's and ψ_j's as in Figure 3.3, we computed all the coefficients numerically, and these are in Table 3.1. Therefore the reduced system (3.14) can be rewritten as the following:

$$\begin{cases} \dot{u}_0 = \tilde{\sigma} u_0 - \sum h^0_{i_0 i_1 i_2} \, u_0^{i_0} u_1^{i_1} u_2^{i_2} + \text{ h.o.t.}, \\ \dot{u}_1 = \tilde{\sigma} u_1 - \omega u_2 - \sum h^1_{i_0 i_1 i_2} \, u_0^{i_0} u_1^{i_1} u_2^{i_2} + \text{ h.o.t.}, \\ \dot{u}_2 = \tilde{\sigma} u_2 + \omega u_1 - \sum h^2_{i_0 i_1 i_2} \, u_0^{i_0} u_1^{i_1} u_2^{i_2} + \text{ h.o.t.}, \end{cases} \tag{3.16}$$

where the summations are over nonnegative integers i_0, i_1, i_2 such that $i_0 + i_1 + i_2 = 3$ and *h.o.t.* means *higher order terms*. We rewrite (3.16) in the compact form

$$\dot{u} = \tilde{\sigma} u + \omega \cdot Tu + H(u) + \text{h.o.t.}, \tag{3.17}$$

where

$$Tu = \begin{pmatrix} 0 & 0 & 0 \\ 0 & 0 & -1 \\ 0 & 1 & 0 \end{pmatrix} \cdot \begin{pmatrix} u_0 \\ u_1 \\ u_2 \end{pmatrix} \tag{3.18}$$

and $H(u)$ is the vector-valued homogeneous cubic polynomials of u_0, u_1, u_2 in (3.16), including the minus sign.

3.3 Derivation of the Normal Form

3.3.1 Elimination of the nonresonant terms

To investigate the dynamics of the reduced system (3.16), following [24] we perform a polynomial transformation of coordinates to obtain its normal form. Let $\mathbb{H}_3$ be

the space of homogeneous polynomials of degree 3. We can regard $H(u)$ in equation (3.17) as an element in the space $\mathbb{H}_3 \oplus \mathbb{H}_3 \oplus \mathbb{H}_3 = \overrightarrow{\mathbb{H}_3}$, a basis of which is given by

$$\left\{u_1^3,\, u_1^2u_2,\, u_1^2u_0,\, u_1u_2^2,\, u_1u_2u_0,\, u_1u_0^2,\, u_0^3,\, u_1^2u_0,\, u_1u_0^2,\, u_0^3\right\}\otimes\left\{\begin{pmatrix}1\\0\\0\end{pmatrix},\begin{pmatrix}0\\1\\0\end{pmatrix},\begin{pmatrix}0\\0\\1\end{pmatrix}\right\}. \tag{3.19}$$

Consider a transformation of the form

$$(u_0, u_1, u_2) = (v_0, v_1, v_2) + P(v_0, v_1, v_2), \tag{3.20}$$

where $P \in \overrightarrow{\mathbb{H}_3}$ is a vector-valued homogeneous cubic polynomial. We substitute (3.20) into (3.17) to find

$$\dot{v} = \tilde{\sigma}v + \omega \cdot Tv + H(v) + \mathrm{ad}T(P)(v) + \text{h.o.t.}. \tag{3.21}$$

Here the adjoint operator $\mathrm{ad}T(\cdot) : \overrightarrow{\mathbb{H}_3} \to \overrightarrow{\mathbb{H}_3}$ in above equation is defined by

$$\mathrm{ad}\,T(P)(v) = TP(v) - (DP)\cdot Tv, \quad \forall P \in \overrightarrow{\mathbb{H}_3}, \tag{3.22}$$

where $DP = (\partial_j P_i)$ is the 3×3 matrix. We shall write $H(v) = H_1(v) + H_2(v)$, where $H_1 \in \mathrm{Ker}(\mathrm{ad}\,T)$ and $H_2 \in \mathrm{Ran}(\mathrm{ad}\,T)$. Then by an appropriate choice of P such that $\mathrm{ad}\,T(P) = -H_2$, the cubic terms $H(v) + \mathrm{ad}\,T(P)(v)$ will reduce to $H_1(v)$, i.e. the projection of the $H(v)$ onto the kernel $\mathrm{Ker}(\mathrm{ad}\,T)$.

To carry out this reduction, we let $\mathrm{ad}\,T(\cdot)$ defined in (3.22) act on each vector of the basis (3.19) and expand the result in the same basis to find $\mathrm{ad}\,T(\cdot)$ has the following matrix

$$\mathrm{ad}\,T = \begin{pmatrix} \mathbb{S}_{10} & \mathbb{O} & \mathbb{O} \\ \mathbb{O} & \mathbb{S}_{10} & -\mathbb{I}_{10} \\ \mathbb{O} & \mathbb{I}_{10} & \mathbb{S}_{10} \end{pmatrix}, \tag{3.23}$$

where $\mathbb{I}_{10}$ is 10 dimensional identity matrix, $\mathbb{O}$ is the 10×10 zero matrix and

$$\mathbb{S}_{10} = \begin{pmatrix} 0 & -1 & 0 & 0 & 0 & 0 & 0 & 0 & 0 & 0 \\ 3 & 0 & 0 & -2 & 0 & 0 & 0 & 0 & 0 & 0 \\ 0 & 0 & 0 & 0 & -1 & 0 & 0 & 0 & 0 & 0 \\ 0 & 2 & 0 & 0 & 0 & 0 & -3 & 0 & 0 & 0 \\ 0 & 0 & 2 & 0 & 0 & 0 & 0 & -2 & 0 & 0 \\ 0 & 0 & 0 & 0 & 0 & 0 & 0 & 0 & -1 & 0 \\ 0 & 0 & 0 & 1 & 0 & 0 & 0 & 0 & 0 & 0 \\ 0 & 0 & 0 & 0 & 1 & 0 & 0 & 0 & 0 & 0 \\ 0 & 0 & 0 & 0 & 0 & 1 & 0 & 0 & 0 & 0 \\ 0 & 0 & 0 & 0 & 0 & 0 & 0 & 0 & 0 & 0 \end{pmatrix}. \tag{3.24}$$

Using Maple to investigate matrix (3.23), we find that $\operatorname{ad} T$ is diagonalizable (in the complex sense) and its nullspace is a six dimensional subspace of $\overrightarrow{\mathbb{H}_3}$ spanned by the following eigenvectors:

$$\begin{pmatrix} r^2 v_0 \\ 0 \\ 0 \end{pmatrix}, \begin{pmatrix} v_0^3 \\ 0 \\ 0 \end{pmatrix}, \begin{pmatrix} 0 \\ r^2 v_1 \\ r^2 v_2 \end{pmatrix}, \begin{pmatrix} 0 \\ v_1 v_0^2 \\ v_2 v_0^2 \end{pmatrix}, \begin{pmatrix} 0 \\ -r^2 v_2 \\ r^2 v_1 \end{pmatrix}, \begin{pmatrix} 0 \\ -v_2 v_0^2 \\ v_1 v_0^2 \end{pmatrix}, \tag{3.25}$$

where for convenience we defined $r = r(v) = \sqrt{v_1^2 + v_2^2}$. On the other hand, the remaining twenty-four eigenvectors of $\operatorname{ad} T$ corresponding to nonzero eigenvalues span the range of $\operatorname{ad} T$ and can therefore be transformed away by an appropriate choice of P in (3.20). Thus the system (3.14) can be transformed to the following simplified form :

$$\begin{cases} \dot{v_0} = \tilde{\sigma} v_0 + a_1 r^2 v_0 + a_2 v_0^3 + \text{h.o.t.}, \\ \dot{v_1} = \tilde{\sigma} v_1 + \omega v_1 + b_1 r^2 v_1 + b_2 v_1 v_0^2 - c_1 r^2 v_2 - c_2 v_2 v_0^2 + \text{h.o.t.}, \\ \dot{v_2} = \tilde{\sigma} v_2 - \omega v_2 + b_1 r^2 v_2 + b_2 v_2 v_0^2 + c_1 r^2 v_2 + c_2 v_1 v_0^2 + \text{h.o.t.}. \end{cases} \tag{3.26}$$

Using Maple to perform the computations, we find that the coefficients in Table 3.1 lead to a reduced system (3.26) with the coefficients $a_{1,2}$, $b_{1,2}$ and $c_{1,2}$ given in Table 3.2.

Table 3.2: The value of the coefficients in the computed normal form (3.26).

a_1	a_2	b_1	b_2	c_1	c_2
0.083	-0.096	-0.130	-0.422	0.003	-0.090

3.3.2 Scaling of the remaining terms

We introduce polar coordinates such that $v_1 = r\cos\theta$ and $v_2 = r\sin\theta$ and for convenience we define $z = v_0$. Then the system (3.26) can be rewritten as the following

$$\begin{cases} \dot{z} = z(\tilde{\sigma} + a_1 r^2 + a_2 z^2) + \mathcal{O}(|r,z|^4), \\ \dot{r} = r(\tilde{\sigma} + b_1 r^2 + b_2 z^2) + \mathcal{O}(|r,z|^4), \\ \dot{\theta} = \omega + \mathcal{O}(|r,z|^2). \end{cases} \tag{3.27}$$

We study the reduced bifurcation problem in the variables r and z. By scaling these variables

$$\tilde{z} = z \cdot \sqrt{-a_2}, \quad \tilde{r} = r \cdot \sqrt{-b_1}, \tag{3.28}$$

we may reduce this subsystem of (3.27) to the *normal form*

$$\begin{cases} \frac{d}{dt}\tilde{z} = \tilde{z}(\tilde{\sigma} - m\tilde{r}^2 - \tilde{z}^2) + \mathcal{O}(|\tilde{r},\tilde{z}|^4), \\ \frac{d}{dt}\tilde{r} = \tilde{r}(\tilde{\sigma} - n\tilde{z}^2 - \tilde{r}^2) + \mathcal{O}(|\tilde{r},\tilde{z}|^4), \end{cases} \tag{3.29}$$

where

$$m = \frac{a_1}{b_1} \approx -0.64, \quad \text{and} \quad n = \frac{b_2}{a_2} \approx 4.40. \tag{3.30}$$

Since to lowest order $\dot{\theta}$ is a constant, an equilibrium of (3.29) with $r \neq 0$ corresponds to a periodic solution of (3.27).

3.4 Analysis of the Bifurcation

In previous sections for the case $\Lambda^{-1} = \Lambda_c^{-1}$ exactly, we derived equation (3.27) for the restriction of (3.3) to the center manifold. Let us show that Equation (3.27) undergoes both a Hopf bifurcation and steady state bifurcation as $\tilde{\sigma}$ passes through

zero. Motivated by [34, 23], we expect that interactions between the two modes can lead to secondary bifurcations.

Neglecting the h.o.t. in (3.29) and dropping the tildes on $\tilde{r}$, $\tilde{z}$, we obtain the system

$$\begin{pmatrix} \dot{z} \\ \dot{r} \end{pmatrix} = f(z, r, \tilde{\sigma}) = \begin{pmatrix} z(\tilde{\sigma} - mr^2 - z^2) \\ r(\tilde{\sigma} - nz^2 - r^2) \end{pmatrix}. \tag{3.31}$$

Note that this system has $\mathbb{Z}_2 \oplus \mathbb{Z}_2$ symmetry under the transformations $z \to -z$ and $r \to -r$. This symmetry helps in the enumeration of equilibria $f(r, z, \tilde{\sigma}) = 0$ of (3.31). Specifically, we have the four possible cases

- the trivial zero solution $(0, 0)$;
- a pure z–mode $(\pm\sqrt{\tilde{\sigma}}, 0)$, corresponding to a standing wave solution;
- a pure r–mode $(0, \sqrt{\tilde{\sigma}})$, corresponding to a periodic solution of (3.27);
- mixed mode which satisfies

$$\tilde{\sigma} = mr^2 + z^2 = nz^2 + r^2. \tag{3.32}$$

The pure z–mode and the pure r–mode appear only while $\tilde{\sigma} \geq 0$, i.e., both modes bifurcate supercritically. Regarding possible mixed modes, given m and n as in (3.30) there is no value of $\tilde{\sigma}$ for which (3.32), a pair of linear equation in r^2 and z^2, has real nonzero solutions. Checking the eigenvalues of $df(z, r, \tilde{\sigma})$, we find when $\tilde{\sigma} < 0$, the trivial zero solution is stable; and when $\tilde{\sigma} > 0$, only the pure z–mode is stable. We summarize this information in the schematic bifurcation diagram Figure 3.4, where a solid line means stable and dashed line means unstable.

More generally, we assume Λ^{-1} in (2.1) is close to, but not exactly equal to, Λ_c^{-1}. As illustrated in Figure 2.1, changing Λ^{-1} shifts both Ω_0 and Re $\Omega_{1,2}$ (in Figure 2.1 the fiber length ℓ is 15, for $\ell = 6$ the graph is very similar). To model these shifts

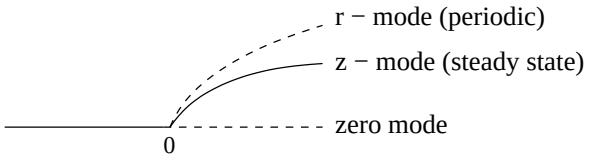

FIGURE 3.4: Schematic bifurcation diagram to the system (3.29), where the horizontal direction denotes the value of $\tilde{\sigma}$. The z–mode represents a symmetric pair of steady solutions of (3.27), and the r–mode represents a periodic solution of (3.27). A solid line means the mode is stable, and a dashed line means it is unstable.

we consider an unfolding[22, 27] of (3.31) with two auxiliary parameters μ_1 and μ_2:

$$\begin{pmatrix} \dot{z} \\ \dot{r} \end{pmatrix} = \begin{pmatrix} z(\tilde{\sigma} - \mu_1 - mr^2 - z^2) \\ r(\tilde{\sigma} - \mu_2 - nz^2 - r^2) \end{pmatrix}. \tag{3.33}$$

Letting $\bar{\sigma} = \tilde{\sigma} - \mu_2$ and $\mu = \mu_1 - \mu_2$, we may eliminate an inessential parameter and rewrite (3.33) in the following form:

$$\begin{pmatrix} \dot{z} \\ \dot{r} \end{pmatrix} = F(z, r, \bar{\sigma}, \mu) = \begin{pmatrix} (\bar{\sigma} - \mu)z - mr^2 z - z^3 \\ \bar{\sigma} r - nrz^2 - r^3 \end{pmatrix}. \tag{3.34}$$

As above, we can enumerate equilibria of (3.34) — solutions of $F(z, r, \bar{\sigma}, \mu) = 0$ — in four cases.

- the trivial zero solution $(0, 0)$;
- for $\bar{\sigma} > \mu$, a pure z–mode $(\pm\sqrt{\bar{\sigma} - \mu}, 0)$, corresponding to a standing wave solution;
- for $\bar{\sigma} > 0$, a pure r–mode $(0, \sqrt{\bar{\sigma}})$, corresponding to a periodic solution;
- a mixed mode which satisfies $\bar{\sigma} = mr^2 + z^2 + \mu = nz^2 + r^2$.

The stability of the bifurcating solutions and the existence of (real) mixed-mode solutions depend on the sign of μ.

Case I : $\mu < 0$. In this case there are no mixed-mode solutions for any value of $\bar{\sigma}$. Thus the equilibria of (3.34) trace out a bifurcation diagram as sketched in Figure 3.5A. Exchange of stability suggests that the trivial solution for $\bar{\sigma} < \mu$ and the z–mode for $\bar{\sigma} > \mu$ are stable and other solutions are unstable. This is easily confirmed from the Jacobian of (3.34).

Case II : $\mu > 0$. In this case, the mixed-mode equations may be solved to obtain

$$r^2 = \frac{(n-1)\bar{\sigma} - n\mu}{mn-1}, \quad z^2 = \frac{(m-1)\bar{\sigma} + \mu}{mn-1}. \tag{3.35}$$

In the range $\delta_1 < \bar{\sigma} < \delta_2$, where

$$\delta_1 = \frac{\mu}{1-m} \quad \text{and} \quad \delta_2 = \frac{n\mu}{n-1}, \tag{3.36}$$

both right-hand-sides of (3.35) are positive. Thus (real) mixed-mode solutions exist for this range of $\bar{\sigma}$. Since $z \to 0$ as $\bar{\sigma} \to \delta_1^+$ and $r \to 0$ as $\bar{\sigma} \to \delta_2^-$, the mixed-mode solution branch connects the pure r– and z–modes, as sketched in Figure 3.5B. Exchange of stability suggests the stability assignments of the figure, and these are readily verified. Speaking teleologically, we may say that the secondary bifurcations of the mixed-mode solution are needed for the primary branches to have the same stability as in Figure 3.4 for large $\bar{\sigma}$.

These bifurcation diagrams agree with the simulations. For fixed $\Lambda^{-1} < \Lambda_c^{-1}$, when we increase σ from 0, the simulations in Figure 3.1 show a steady state bifurcation from the trivial solution to a standing wave solution, which is the behavior in the bifurcation diagram Figure 3.5A. For fixed $\Lambda^{-1} > \Lambda_c^{-1}$, when we increase σ from 0, Figure 3.1 shows we first encounter a bifurcation from the trivial solution to a pure r–mode (periodic solution with zero average, to leading order), and then it bifurcates to a mixed mode (periodic solution with nonzero average), finally it bifurcates to the pure z–mode (standing wave solution), all of which can be observed from Figure 3.5B as we increases $\bar{\sigma}$.

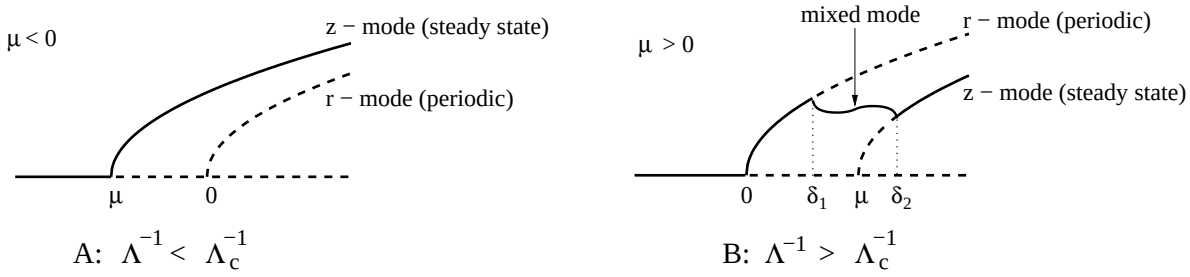

FIGURE 3.5: Schematic bifurcation diagrams for two cases $\Lambda^{-1} < \Lambda_c^{-1}$ and $\Lambda^{-1} > \Lambda_c^{-1}$, where the horizontal direction denotes the value of $\bar{\sigma}$. The solid line means the mode is stable and the dashed line means it is unstable.

The above data also provide a check on the accuracy of truncating all h.o.t.. We can obtain δ_1 and δ_2 from the simulation in Figure 3.2, where $\Lambda^{-1} = 3.3$. δ_1 represents the increase in $\bar{\sigma}$, or equivalently of σ, from the first bifurcation (emergence of the pure r–mode) to the second bifurcation (the appearance of the mixed mode), and similarly δ_2 represents the increase in $\bar{\sigma}$ or σ from the first bifurcation to the third. We find

$$\delta_1\big|_{\text{sim}} \approx 3.32 - 3.14 = 0.18, \quad \delta_2\big|_{\text{sim}} \approx 3.49 - 3.14 = 0.35.$$

On the other hand, since $\mu = \mu_1 - \mu_2$, where to the leading order μ_1 and μ_2 are shifts of the threshold values of $\tilde{\sigma}$ for the emergence of pure z–mode and r–mode respectively, we obtain $\mu = \text{Re}\ \Omega_1 - \Omega_0$. By computation of the eigenvalues, when $\Lambda^{-1} = 3.3$, we have $\mu \approx 0.28$. Thus the formula in (3.36) gives the theoretical result:

$$\delta_1\big|_{\text{th}} = \frac{\mu}{1-m} \approx 0.17, \quad \delta_2\big|_{\text{th}} = \frac{n\mu}{n-1} \approx 0.36$$

for the values of m and n in (3.30), which matches the simulated result well.

3.5 Summary

In this Chapter we have studied the bifurcations of the modulation equation (2.1) for APD alternans propagating on a cardiac fiber. We observed the solutions undergo

either a steady state or a Hopf bifurcation; which occurs first depends on one parameter in the equation, the nondimensional Λ^{-1} defined in (2.6). There is one special value Λ_c^{-1} so that we have a codimension two bifurcation for $\Lambda^{-1} = \Lambda_c^{-1}$; if Λ^{-1} is near Λ_c^{-1}, there is competition between multiple modes, which leads to the following: 1) for $\Lambda^{-1} < \Lambda_c^{-1}$, the equation (2.1) has a simple steady state bifurcation as we increase the bifurcation parameter σ; 2) for $\Lambda^{-1} > \Lambda_c^{-1}$ we will encounter a Hopf bifurcation followed by secondary bifurcations and finally we will reach a standing wave solution for σ sufficiently large.

We also observe an interesting phenomenon: the amplitude of alternans at the stimulus site is quite different for the steady state and the periodic solution. For instance, the pure z–mode (standing wave solution, as shown in Fig 3.1B, upper graph) has an nonzero constant value at the stimulus site, but the pure r–mode solution (pure periodic, as shown in Fig 3.1B, bottom) almost has no amplitude of oscillation at $x = 0$. This can be seen from the eigenfunctions $\phi_j's$ (see Figure 3.3A). The z–mode is approximately given by ϕ_0 and the r–mode, by $\phi_{1,2}$. The different behavior between ϕ_0 and $\phi_{1,2}$ induces the great change of the amplitude of solution at $x = 0$.

Throughout this Chapter, the dimensionless cardiac fiber length is assumed to be $\ell = 6$. However, the dynamical behavior of (2.1) is similar for arbitrary ℓ which is not too small. In particular, the evolution of eigenvalues has the same behavior as in Figure 2.1 when we increase Λ^{-1}.

For Λ^{-1} in a broader neighborhood of Λ_c^{-1}, possibly far away from Λ_c^{-1}, (2.1) may have more complicated dynamics, including chaos, which we shall show in the next Chapter.

4

Chaos at Extreme Parameter Values

In this chapter, we discuss the chaotic solution we observe in the modulation equation (2.1) for the parameters at extreme values.

It is believed that ventricular fibrillation in cardiac tissue represents chaotic behavior [60]. Mathematically, chaos has been seen in spiral and scroll waves in an excitable medium [3, 48] in two- and three-dimensional case. We find that, for some range of the parameters in the Echebarria-Karma modulation equation (2.1), the solution is chaotic. The chaotic alternans we find exists in one dimension, which shows a possible different mechanism from those in higher dimensions such as spiral and scroll waves.

Throughout this chapter, we assume the cardiac fiber length $\ell = 15$ and the dispersive coefficient $\Lambda^{-1} = 10$ (both in dimensionless units). We investigate the behavior of the solution to (2.1) for various values of σ by numerically solving the equation. The numerical method we employ is to combine operator splitting and a linear implicit solver. The fiber is discretized by finite difference method with spatial step $dx = 0.075$, i.e. we have mesh points $x_{i-\frac{1}{2}} = (i-0.5)\,dx$ for $i = 0, 1, \ldots, 200, 201$.

The Neumann boundary conditions (2.2) imply

$$a(x_{-\frac{1}{2}},t) = a(x_{\frac{1}{2}},t) \quad \text{and} \quad a(x_{200-\frac{1}{2}},t) = a(x_{201-\frac{1}{2}},t) \tag{4.1}$$

for all the time t. For the simulations in Figure 4.1, 4.2, 4.3, 4.6 and 4.7 we use time step $dt = 0.002$. And in the simulations in Figure 4.4 and 4.5 we choose various values of dt for exploration.

In Figure 4.1 we show a phase-plane representation of the solutions to (2.1) for several different values of σ, choosing two fixed positions y_1 and y_2 on the fiber and then plotting $a(y_2,t)$, $a(y_1,t)$ as time evolves. For instance in Figure 4.1, we use $y_1 = x_{150-\frac{1}{2}}$ and $y_2 = x_{170-\frac{1}{2}}$. It appears A is a periodic solution, B is period doubled, and C is possibly chaotic.

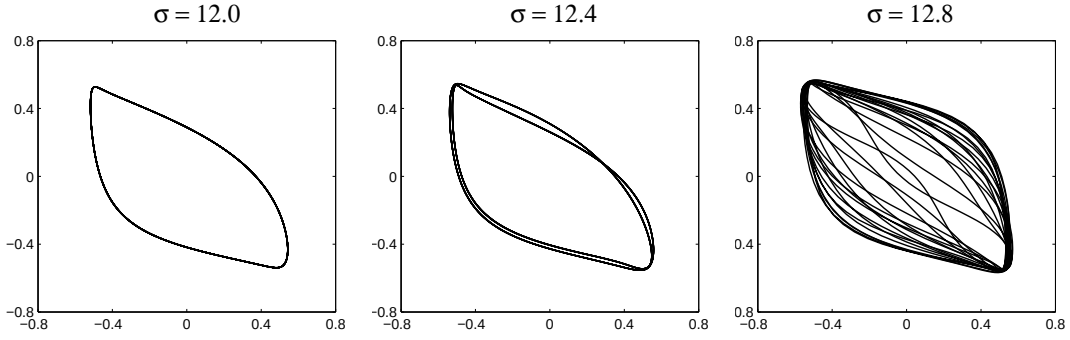

FIGURE 4.1: Phase plane of $a(y_2,t)$ vs $a(y_1,t)$ for three different values of σ, assuming $\ell = 15$ and $\Lambda^{-1} = 10$.

To view the evolution of the dynamics as σ increases more clearly, we draw the orbit diagram in Figure 4.2, which is obtained by the following steps. For each value of σ, consider the Poincare sectional hyper-plane defined by $a(y_2,\cdot) = 0$. We study the solution of (2.1) in a time range $T_1 < t < T_2$, where $T_1 = 200$ is chosen to eliminate the initial transient and $T_2 = 700$. For times in this interval, if the solution $a(x,t)$ transverses this hyper-plane at some time t_n in the positive direction, i.e. $a(y_2,\cdot)$ increasing from negative to positive at time t_n, we record the value of

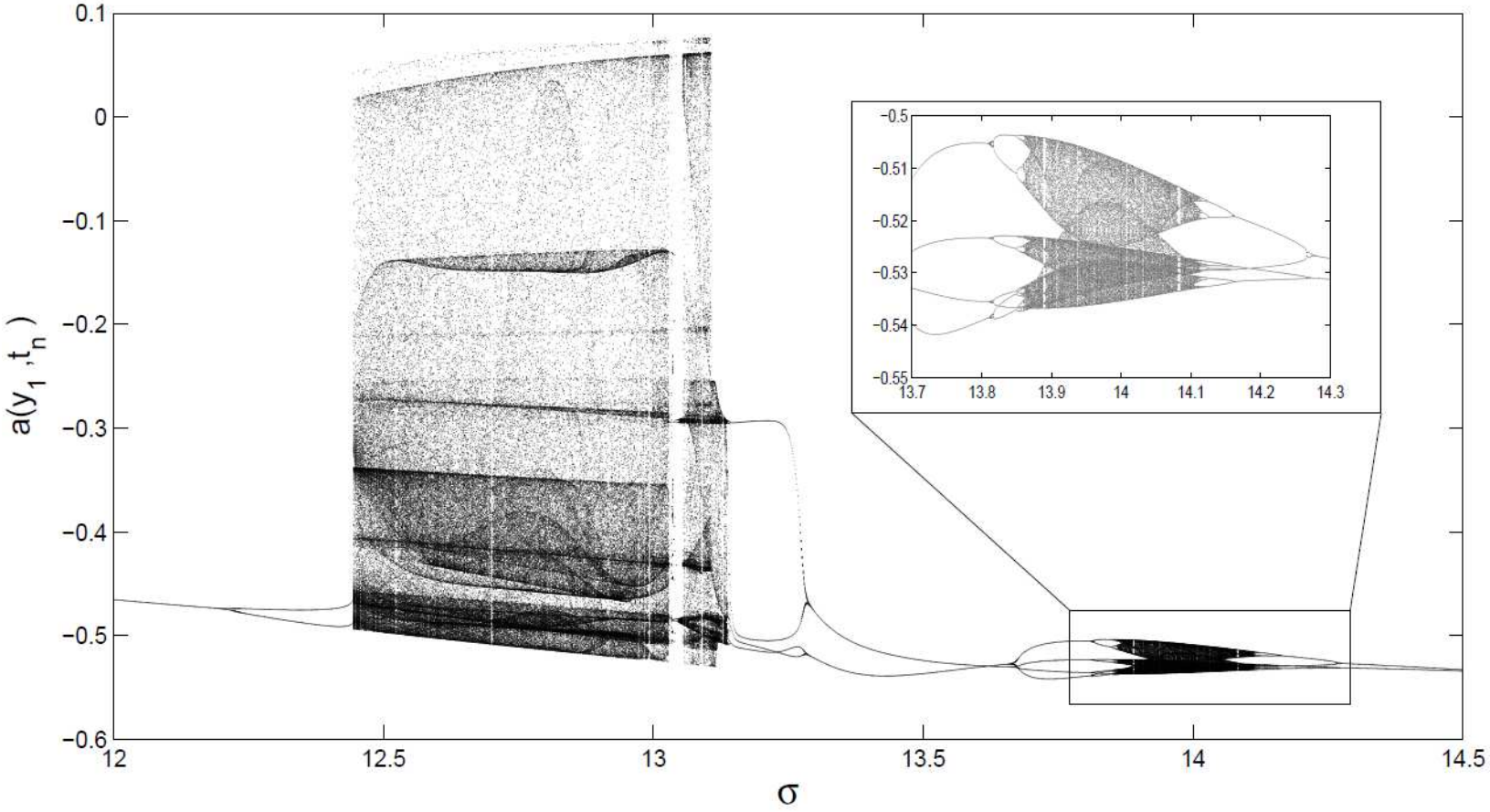

FIGURE 4.2: Orbit diagram for the solution to (2.1) as σ increases, assuming $\ell = 15$ and $\Lambda^{-1} = 10$. The interval between two adjacent σ's is 0.001. As explained in the text, the vertical axis is $a(y_1, t_n)$, where t_n is some time between $T_1 = 200$ and $T_2 = 700$ when $a(y_2, t)$ becomes positive.

$a(y_1, t_n)$ in Figure 4.2. Therefore if the solution is "period-one" as in Figure 4.1A, we obtain one value of $a(y_1, \cdot)$; if the solution is "period-two" as in Figure 4.1B, we obtain two distinct values of $a(y_1, \cdot)$; and if the solution is chaotic as in Figure 4.1C, we expect to obtain a large number of values, depending on the range of time we consider. The orbit diagram in Figure 4.2 is given by plotting all the values of $a(y_1, t_n)$ we obtain versus σ.

From the orbit diagram, we find that as σ increases, there is a period-two bifurcation at around $\sigma = 12.20$, and a bifurcation to intermittent chaos at around $\sigma \approx 12.44$. The intermittency can be observed by plotting the values $a(y_1, t_n)$ versus n in Figure 4.3, where $\sigma = 12.45$ is just beyond the bifurcation value.

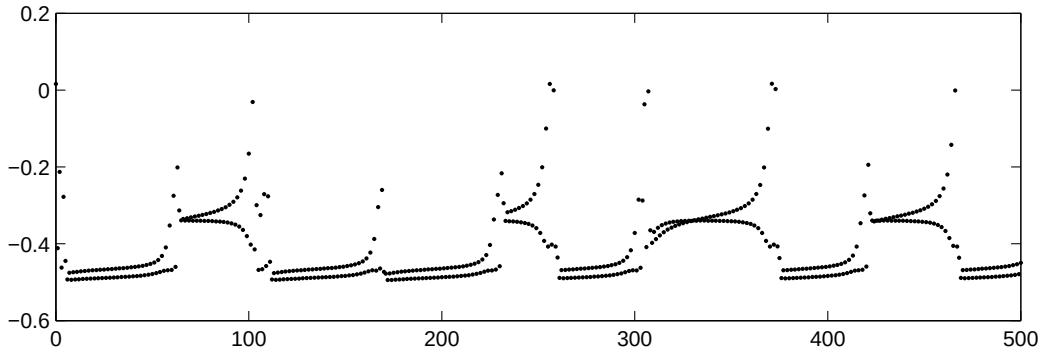

FIGURE 4.3: Plotting of the values $a(y_1, t_n)$ in the Poincare hyperplane versus n, where $\sigma = 12.45$ which is just beyond the bifurcation point. An intermittent pattern is apparent.

We observe that there is a chaotic window $12.45 \lesssim \sigma \lesssim 13.12$ in the orbit diagram. We have examined the range for σ between 13.03 and 13.06, the "gap" in the chaotic window shown in the diagram, in detail. In particular, 1) increasing σ in steps of 10^{-6}, we found various periodic solutions. The period farthest along in the U-sequence was 9 [24, 42]; 2) in certain ranges a period 4 solution was observed at all points, but the precise orbit seemed to jump in a discontinuous fashion.

For σ beyond 13.12, the solution exhibits more transitions between chaotic and

periodic behaviors.

The orbit diagram in Figure 4.2 provides an elementary overview of the behavior of the solution. However, to verify that we do have a chaotic solution indeed, we need more evidence. We study the case $\sigma = 12.8$ in detail in the following.

4.1 Computing the Lyaponuv Exponents

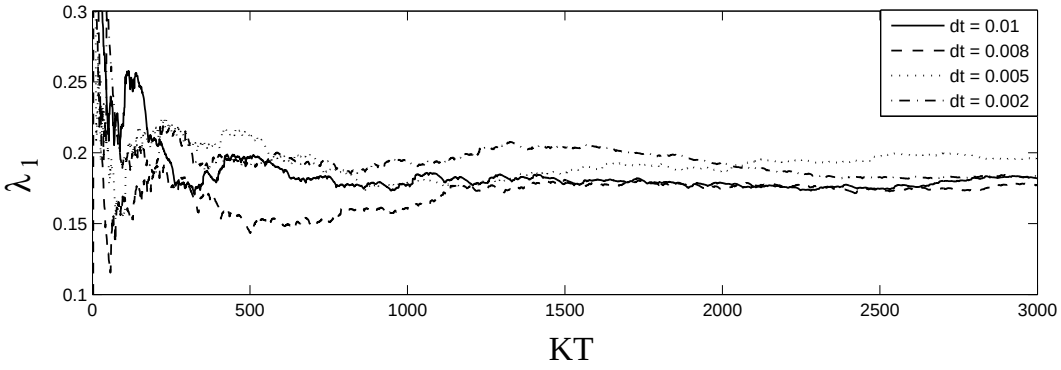

FIGURE 4.4: The first Lyapunov exponent λ_1 versus the total time KT for the computation, where $\ell = 15$, $\Lambda^{-1} = 10$ and $\sigma = 12.8$.

The most straightforward approach to verify chaos is to show the first Lyaponuv exponent of the system is positive [2]. The first Lyaponuv exponent can be simply obtained by considering the variation equation of (2.1), i.e.

$$\partial_t\ \delta a = \sigma\ \delta a + \mathbf{L}\ \delta a - 3ga^2(x,t)\ \delta a, \tag{4.2}$$

where $a(x,t)$ is the solution to equation (2.1). To perform the computation, we choose an initial state $a_0 = a(x,t_0)$ lying on the basin of the attractor and an initial variation $u^{(0)} := \delta a_0$ (usually normalized). For a fixed time length T, we integrate the variation equation (4.2) to obtain δa_1. We then normalize δa_1 to obtain $u^{(1)} = \delta a_1/||\delta a_1||$, where the norm of a function on the fiber $f(x)$ is defined to be the L^2-norm, i.e.

$$||f|| := \left(\int_0^\ell |f(x)|^2\, dx\right)^{1/2}. \tag{4.3}$$

We then integrate the variation equation with initial condition $u^{(1)}$ to obtain δa_2. We repeat the procedure K times, and for K large enough, we obtain the estimate [50]:

$$\lambda_1 \approx \frac{1}{KT} \sum_{j=1}^{K} \ln ||\delta a_j||. \tag{4.4}$$

Figure 4.4 shows the right hand side of (4.4) versus the total time KT for $T = 1$ with different numerical time steps dt. We approximate λ_1 by (4.4) for various values of the numerical time step dt. We find that the first Lyapunov exponent $\lambda_1 \approx 0.2$, which is positive. We also note that the second Lyaponuv exponent λ_2 computed is approximately zero, which matches the theory [24].

For further evidence, Figure 4.5 is a plot of an average of λ_1 versus various numerical time step dt. We observe that there is apparently no trend for λ_1 to vanish for smaller time step.

Also, the computation of λ_1 does not depend on the length of the normalization time interval T, provided T is not too large. To check this we repeated the previous calculation for $T = 1, 2, 4, 8, 16$ with fixed total time KT and observed very little difference.

4.2 Power Spectrum

As supplementary evidence we show that the trajectory has a continuous power spectrum. Specifically, from a sequence $\{t_k\}$ of equally spaced times $\Delta t = 0.1$ (starting after the transient has decayed), we obtain the time sequence $\{a(y_1, t_k)\}$. In practice, we collect 2048 values of $a(y_1, t_k)$ in total. Then we perform a discrete Fourier transformation to the time sequence $\{a(y_1, t_k)\}$ and compute the amplitude for each frequency. Figure 4.6 shows a plot of the logarithm of the amplitude versus the frequency (solid curve), where each value has been averaged by its 10 nearest neighbors.

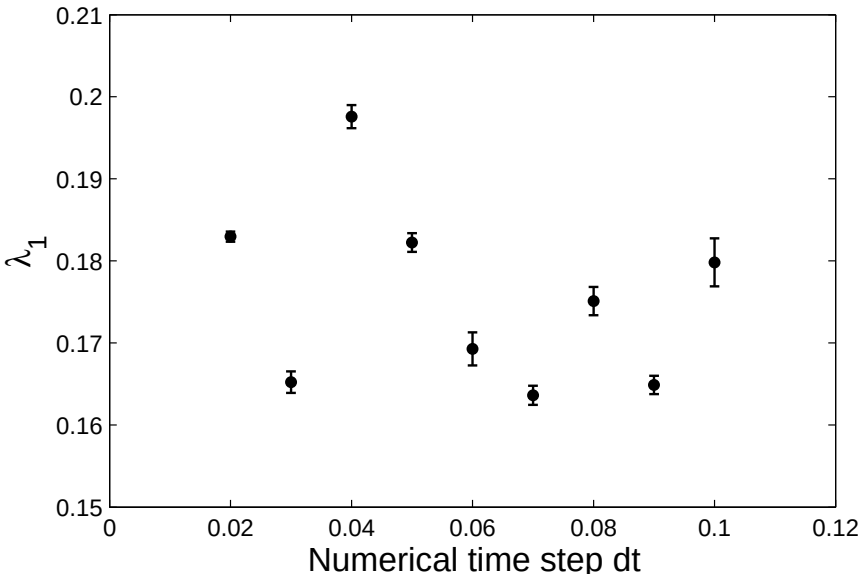

FIGURE 4.5: The averaged first Lyapunov exponent λ_1 during $2500 \leq KT \leq 3000$ versus numerical time step dt, where $\ell = 15$, $\Lambda^{-1} = 10$ and $\sigma = 12.8$.

We observe that the spectrum has a continuous pattern.

For comparison, we plot the instrumentally sharp spectrum on the same graph (dashed curve, only first harmonic is plotted), which is generated by the following. We consider the pure periodic time sequence $\{A\cos(\omega t_k)\}$, where ω is the frequency of the power spectrum of $\{a(y_1, t_k)\}$ with largest amplitude (cf. Figure 4.6), and A is the corresponding amplitude. We then obtain the power spectrum of $\{A\cos(\omega t_k)\}$ with the same process. The peaks of the instrumentally sharp spectrum are apparent and isolated, which is definitely different from that of $\{a(y_1, t_k)\}$.

4.3 The correlation dimension of the attractor

Further information is provided by the correlation dimension of the attractor of the trajectory. We calculate the correlation dimension following [2, 55]. Below we will choose many "base points". Such points can be obtained by letting the system evolve for a long time such that the transient decays. Let p be one such point. We

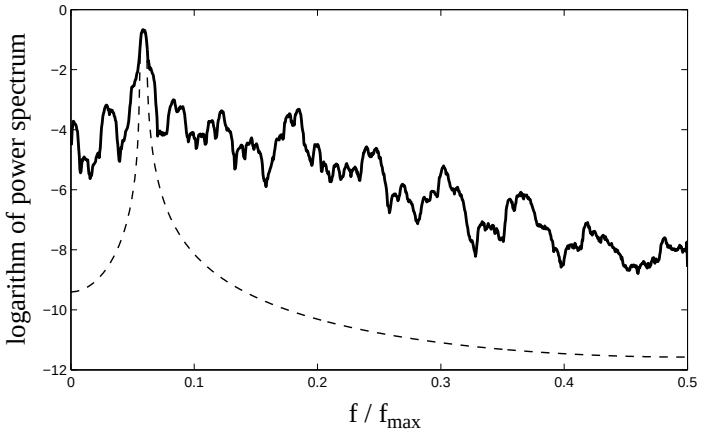

FIGURE 4.6: Plot of the logarithm of the power spectrum versus the frequency. The solid curve is for the solution $a(y_1, t_k)$ with fixed position $y_1 = x_{150-\frac{1}{2}}$ and total 2048 discrete t_k's by time interval 0.1, assuming $\ell = 15$, $\Lambda^{-1} = 10$ and $\sigma = 12.8$; the dashed curve is the instrumentally sharp spectrum.

consider a ball $B_p(\epsilon)$ centered at p with radius ϵ. Here the distance of two solutions at time t, $a(x,t)$ and $b(x,t)$, is given by the $L^2(0,\ell)$-norm. Then we pick a fixed large number of random points on the trajectory (which is also very close to the attractor). We are interested in those points located in the ball $B_p(\epsilon)$, the number of which is denoted by $n(\epsilon)$. If the attractor is D-dimensional, we expect $n(\epsilon)$ to be approximately proportional to ϵ^D, i.e. there is some constant C such that

$$n(\epsilon) \approx C\,\epsilon^D. \tag{4.5}$$

In case that the solution is periodic, the dimension of the attractor D is exactly 1. To find the dimension, we rewrite (4.5) in the following form,

$$\ln(n(\epsilon)) \approx D\ln(\epsilon) + \ln C, \tag{4.6}$$

i.e. the $\ln(n(\epsilon))$ is expected to be a linear function of $\ln(\epsilon)$ with slope D. Therefore, we pick $\epsilon_k = 2^{-k}\epsilon_0$ for $k = 0, 1, 2, \ldots$ and find $n(\epsilon_k)$, the number of points falling into the ball $B_p(\epsilon_k)$ for each k. And we may plot $\ln(n_k)$ versus $\ln(\epsilon_k)$ and approximate the coefficient D by interpolation.

As mentioned above, for better accuracy, instead of considering one base point p, we pick 1000 base points on the attractor. Then we generate 5×10^5 points on the trajectory, which is a time sequence with equal time interval ΔT. For given ϵ and each ball centered at j-th base point, let $n_j(\epsilon)$ be the number of those points falling into the j-th ball. We take $n(\epsilon)$ to be the average of all $n_j(\epsilon)$'s over the total 100 balls. We plot $\ln(n(\epsilon_k))$ versus $\ln(\epsilon_k)$ in Figure 4.7. For the case labelled $N = 200$ we find that the correlation dimension $D \approx 2.052 \pm 0.027$. The standard deviation in D arises from the simple linear regression method, which assumes the errors are independent Gaussians.

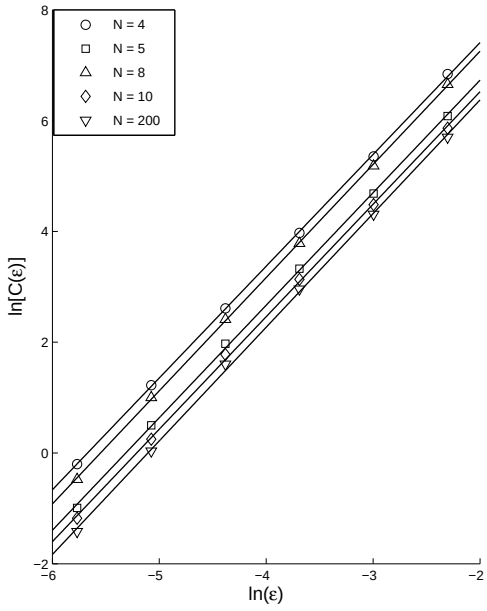

FIGURE 4.7: Plot of the logarithm of $C(\epsilon)$, the average of number of points on the trajectory falling into the ϵ-balls, versus logarithm of ϵ, for various N, the number of spatial subintervals in approximating the $L^2(0, \ell)$-norm in (4.3). Note that in the cases of $N = 20, 25, 40, 50, 100$, the plots are very close to the case $N = 200$ and hard to distinguish. Therefore they are not plotted individually.

We now explain the meaning of N in Figure 4.7 and Table 4.1. In the above calculation, the distance between two "points", which are in fact two functions $a(\cdot, t_1)$ and

$a(\cdot, t_2)$, is defined by the $L^2(0, \ell)$-norm. In the numerical simulation, we only have the function values on the spatial mesh points, i.e. $a(x_{j-\frac{1}{2}}, t)$ for $j = 0, 1, \ldots, 200, 201$. With trapezoidal rule, we find the $L^2(0, \ell)$-norm defined in (4.3) is approximated by

$$||a(\cdot, t)|| = \left(\int_0^\ell |a(x,t)|^2 \, dx \right)^{1/2} \approx \sqrt{dx} \left(\sum_{i=1}^{200} a(x_{i-\frac{1}{2}}, t)^2 \right)^{1/2}, \tag{4.7}$$

where we have used the boundary conditions (4.1). Therefore up to a constant factor, the $L^2(0, \ell)$-norm is equal to the Euclidean distance of points in a 200-dimensional Euclidean space. For comparison, we also consider calculating the norm using only a subgrid. To avoid unnatural interpolation, we consider only subgrids with values of N that divide 200. The data are plotted in Figure 4.7 and the dimension D is summarized in Table 4.1. We find that in all cases, D is nearly 2.

Table 4.1: The correlation dimension of the attractor of the solution to (2.1) for various N, the number of spatial subintervals in approximating $L^2(0, \ell)$-norm in (4.3), assuming $\ell = 15$, $\Lambda^{-1} = 10$ and $\sigma = 12.8$.

N	Dimension
2	2.054 ± 0.013
4	2.018 ± 0.012
5	2.031 ± 0.020
8	2.043 ± 0.012
10	2.031 ± 0.021
20	2.049 ± 0.026
25	2.048 ± 0.025
40	2.051 ± 0.027
50	2.052 ± 0.027
100	2.052 ± 0.027
200	2.052 ± 0.027

4.4 Discussion

We have studied numerically one chaotic solution of the modulation equation (2.1) for APD alternans propagating on a cardiac fiber, specifically when the parameter

$\ell = 15$, $\Lambda^{-1} = 10$ and $\sigma = 12.8$. We verified that this solution is indeed chaotic by the following evidence: (i) the first Lyaponuv exponent of the system is positive, (ii) the power spectrum is continuous, (iii) the correlation dimension of the attractor is close to 2. The above observations are the universal properties for the chaotic solutions we obtained for various values of the parameters. For instance Table 4.2 shows the correlation dimension of the attractor if the length of the fiber ℓ is different. In all cases we keep $\Lambda^{-1} = 10$ and $\sigma = 12.8$ and the solutions are all chaotic and we use the $L^2(0, \ell)$-norm in computing the distance between trajectories. We observe that the dimension does not apparently increase with ℓ. As we mentioned before, in estimating the dimensions, the errors are assumed to be independent Gaussians by the linear regression. Of course this assumption need not hold; indeed, there may even be nonrandom systematic errors, especially for intermittent chaos. Thus the actual errors could significantly exceed these estimates. Therefore we do not attach great significance to the two low dimensions in Table 4.2.

Table 4.2: The correlation dimension of the attractor of the solution to (2.1) for various ℓ, assuming $\Lambda^{-1} = 10$ and $\sigma = 12.8$.

length ℓ	Dim D
6	2.020 ± 0.025
9	1.992 ± 0.031
12	1.939 ± 0.012
15	2.052 ± 0.027
18	1.935 ± 0.010
21	2.099 ± 0.030

We note that the Lyaponuv dimension,

$$D_L = k + \frac{\lambda_1 + \lambda_2 + \ldots + \lambda_k}{|\lambda_{k+1}|}, \tag{4.8}$$

where λ_j's are the Lyaponuv exponents and k the maximum value of j such that $\lambda_1 + \lambda_2 + \ldots + \lambda_j > 0$, as defined in [30], is always greater than 2. The Kaplan-

Yorke Conjecture [19, 30] states that the Lyaponuv dimension equals the correlation dimension. There has not been a general proof so far, however, in some cases it was proved [35, 62].

5

Conclusion and Discussion

The Echebarria-Karma modulation equation (2.1) provides a description of the evolution of the amplitude of alternans along a cardiac fiber under rapid pacing. In this thesis, we present the following contributions.

In Chapter 2, we consider the spectrum of the linearized operator of the spatial part of the modulation equation (2.1). In particular, the first eigenvalue $\Omega_{\max}$ (the one with the largest real part) determines the type of bifurcation we have from the zero trivial solution when we increase the parameter σ from 0 (the practical meaning is to reduce the BCL of pacing below the critical value B_{c}). If $\Omega_{\max}$ is real, we have a steady-state bifurcation; if $\Omega_{\max}$ is complex, we have a Hopf bifurcation. For a given cardiac fiber with fixed length which is not short, the bifurcation we encounter is determined by whether Λ^{-1} is larger or smaller than a critical value Λ_c^{-1} where the first eigenvalue $\Omega_{\max}$ becomes complex. In case of long fiber, we compute the critical value Λ_c^{-1} asymptotically in (2.81). We also verify our findings by simulations of the two-current model and the Noble model.

In Chapter 3, we focus on the bifurcations that occur when Λ^{-1} is around the critical value Λ_c^{-1}. We investigate the competition between the steady-state and

Hopf modes, both numerically and analytically. When Λ^{-1} is exactly Λ_c^{-1}, we use center manifold theory to reduce the equation to a dynamical system on a three-dimensional center manifold and obtain its normal form and its bifurcations. Then we consider the cases when Λ^{-1} is close to, but not exactly equal to Λ_c^{-1}. We apply the unfolding theory and do the bifurcation analysis to find that at sufficiently rapid pacing (but assuming a 1:1 response is maintained), i.e. for σ sufficiently large, steady patterns always emerge as the only stable solution. However, in the parameter range where Hopf bifurcation occurs first, the evolution from periodic solution (just after the bifurcation) to the eventual standing wave solution occurs through a series of secondary bifurcations.

In Chapter 4, we illustrate and verify the existence of chaotic solution to the modulation equation, which provides an alternative mechanism of the cardiac chaos than those known before. We use the solution when $\ell = 15$, $\Lambda^{-1} = 10$ and $\sigma = 12.8$ as an example and verify that this solution is chaotic by computing the first Lyapunov exponent numerically. We also calculated the power spectrum and the correlation dimension of the attractor of the system as an auxiliary evidence.

Appendix A

Dispersion Curve for the Two-current Model

In this appendix, we show that for the cable equation of the two-current model (1.19)–(1.20), the dispersion curve is given by (1.21) to leading order.

Let us summarize the evolution of the voltage and gate during a series of action potential, the details of which can be found in [43]. In the two-current model, the four phases, upstroke, plateau, refractory and recovery, occur over time scales $\mathcal{O}(\tau_{\text{in}})$, $\mathcal{O}(\tau_{\text{close}})$, $\mathcal{O}(\tau_{\text{out}})$ and $\mathcal{O}(\tau_{\text{open}})$ respectively. By the assumption (1.12), the time scales for the upstroke and refractory phase are much smaller than the other two. In the upstroke phase for $(n+1)$-th action potential, the voltage quickly rises to its peak value

$$v_+(D_n) = \frac{1}{2}\left(1 + \sqrt{1 - h_{\text{min}}/h_{\text{ini}}(D_n)}\right), \tag{A.1}$$

where

$$h_{\text{min}} = 4\tau_{\text{in}}/\tau_{\text{out}}, \tag{A.2}$$

and

$$h_{\text{ini}}(D_n) = 1 - (1 - h_{\text{min}})e^{-\frac{D_n}{\tau_{\text{open}}}}; \tag{A.3}$$

whereas the gate h keeps at its initial value $h_{\rm ini}(D_n)$ to leading order. In plateau phase, the voltage gradually decreases to 1/2 and the gate decreases to its minimal value $h_{\rm min}$, both to leading order. In refractory phase, the voltage quickly decreases below $v_{\rm crit}$ and tends to zero, whereas the gate keeps approximately at $h_{\rm min}$. In recovery phase, i.e. the $(n+1)$-th diastolic interval, the voltage keeps approximately zero and the gate recovers to $h_{\rm ini}(D_{n+1})$.

We now consider a periodic wave train of action potentials with a constant travelling speed c. At a given position x_0, we denote A_n and D_n to be n-th action potential duration and n-th diastolic interval respectively. To find c, we seek a solution of travelling wave front of (1.19)–(1.20) of the form

$$v(x,t) = V(\eta), \quad h(x,t) = H(\eta), \tag{A.4}$$

where

$$\eta = \frac{1}{\tau_{\rm in}}\left(\frac{x}{c} - t\right). \tag{A.5}$$

The functions $V(\eta)$ and $H(\eta)$ will satisfy a system of ODEs.

In the following, we will focus on the travelling front and reduce the equations to (A.8) to leading order. We will talk discuss the existence of the speed c and then compute it explicitly.

With $V(\eta)$ and $H(\eta)$ in (A.4), equations (1.19)–(1.20) become

$$-\frac{1}{\tau_{\rm in}}V' = \frac{K}{c^2\tau_{\rm in}^2}V'' + \frac{1}{\tau_{\rm in}}HV^2(1-V) - \frac{V}{\tau_{\rm out}} \tag{A.6}$$

and

$$-\frac{1}{\tau_{\rm in}}H' = \begin{cases} -\dfrac{H}{\tau_{\rm close}}, & \text{if } v > v_{\rm crit}; \\ \dfrac{1-H}{\tau_{\rm open}}, & \text{if } v < v_{\rm crit}. \end{cases} \tag{A.7}$$

Since the voltage increases approximately from 0 to $V_+(D_n)$ in the wave front, we require $\lim_{\eta\to+\infty} V(\eta) = 0$ and $\lim_{\eta\to-\infty} V(\eta) = V_+(D_n)$. Recall that the wave front corresponds to the phase of upstroke, which occurs over a time scale of order $\mathcal{O}(\tau_{\text{in}})$, and the change of η during the wave front is $\mathcal{O}(1)$ by (A.5). Thus to leading order H is constant in the layer of the wave front, i.e. to leading order $H = h_{\text{ini}}(D)$ throughout the wave front. Thus (A.6) reduces to

$$\frac{K}{c^2\tau_{\text{in}}}V'' + V' + h_{\text{ini}}(D)V^2(1-V) - \frac{h_{\min}}{4}V = 0, \tag{A.8}$$

which may be rewritten as the following

$$\frac{K}{c^2\tau_{\text{in}}}V'' + V' + h_{\text{ini}}(D)V[V - V_-(D_n)][V - V_+(D_n)] = 0, \tag{A.9}$$

where

$$V_\pm(D_n) = \frac{1}{2}\left(1 \pm \sqrt{1 - h_{\min}/h_{\text{ini}}(D_n)}\right). \tag{A.10}$$

Note that $V_+(D_n)$ is just the peak value of the voltage in the action potential in (A.1). In the following part for convenience we use $V_\pm$ for $V_\pm(D_n)$ in (A.10) and we also use abbreviation h_{ini} for $h_{\text{ini}}(D_n)$ in (A.3).

We show that there exists a value of c that gives a heteroclinic solution. We set $W = V'$ and transform (A.9) into a system of ODEs:

$$V' = W, \tag{A.11}$$

$$W' = \frac{c^2\tau_{\text{in}}}{K}\Big\{ - W + h_{\text{ini}}V(V - V_-)(V - V_+)\Big\}. \tag{A.12}$$

The system (A.11)–(A.12) has three equilibria, $(0,0)$ and $(V_\pm(D_n),0)$ and we are interested in $(0,0)$ and $(V_+,0)$. By calculating the linearization, where we omit the details, we can show that both $(0,0)$ and $(V_+,0)$ are saddles. As shown in [14],

for a unique wave speed c, the unstable manifold of $(0,0)$ coincides with the stable manifold of $(V_+,0)$ and gives a heteroclinic orbit in the V-W phase plane.

In fact c can be computed explicitly. We assume the solution to (A.9) also satisfies the following first order ODE

$$V' = rV(V - V_+), \tag{A.13}$$

where r is a constant to be determined. It turns out that for appropriate r and c, the original equation (A.9) is naturally satisfied. Differentiating (A.13), we obtain

$$V'' = rV'(2V - V_+) = r^2V(V - V_+)(2V - V_+). \tag{A.14}$$

Substituting (A.13) and (A.14) into (A.8) we find

$$V(V - V_+)\left\{V(\frac{2Kr^2}{c^2\tau_{\text{in}}} - h_{\text{ini}}) + (r + h_{\text{ini}}V_- - \frac{Kr^2}{c^2\tau_{\text{in}}}V_+)\right\} = 0 \tag{A.15}$$

Equation (A.15) is satisfied as an identity for all values of V if

$$\frac{2Kr^2}{c^2\tau_{\text{in}}} - h_{\text{ini}} = 0 \tag{A.16}$$

and

$$r + h_{\text{ini}}V_- - \frac{Kr^2}{c^2\tau_{\text{in}}}V_+ = 0. \tag{A.17}$$

Solving (A.16) and (A.17) for r and c, we find

$$r = h_{\text{ini}}(\frac{1}{2}V_+ - V_-), \tag{A.18}$$

and

$$c = \sqrt{\frac{2Kh_{\text{ini}}}{\tau_{\text{in}}}}\left(\frac{1}{2}V_+ - V_-\right). \tag{A.19}$$

By (1.12), we have $h_{\min} \ll h_{\text{ini}}$. Therefore

$$\frac{1}{2}V_+ - V- = \frac{3}{4}\sqrt{1 - h_{\min}/h_{\text{ini}}} - \frac{1}{4} \approx \frac{1}{2} - \frac{3}{8}h_{\min}/h_{\text{ini}}. \tag{A.20}$$

Substituting (A.20) into (A.19) we obtain the dispersion curve $c = c(D_n)$ as in (1.21).

Above we estimated the travelling velocity c of an infinite periodic wave train, which is a function of the local diastolic interval D_n. In the derivation of the Echebarria-Karma equation, the formula in (1.21) is assumed to hold for general modulating waves even though $D_n(x)$ varies in both space and time.

Appendix B

Derivation of the Modulation Equation

In this appendix, we derive (1.37) by expanding the right hand side of (1.36) to lowest order.

Without loss of generality, we assume $n = 0$. Substituting (1.27) and (1.28) into (1.36), we find the right hand side of (1.36) equals

$$\begin{aligned} & f\left[T(x,1) - f\left[T(x,0) - A(x,0)\right]\right] - A(x,0) \\ = \;& f\left[B_c + \delta\tau - b - f\left[\tau_c + \delta\tau + b - (A_c + \delta A + a)\right]\right] - A(x,0) \\ = \;& f\left[B_c + \delta\tau - b - f\left[D_c + \delta\tau - \delta A + b - a\right]\right] - A(x,0). \end{aligned} \tag{B.1}$$

Recalling $B_{\mathrm{c}} - A_{\mathrm{c}} = D_{\mathrm{c}}$, and defining

$$\alpha = \delta\tau - \delta A + b - a, \tag{B.2}$$

and

$$\beta = \delta\tau - b, \tag{B.3}$$

we may rewrite (B.1) as

$$f\left[B_{\mathrm{c}} + \beta - f\left[D_{\mathrm{c}} + \alpha\right]\right] - A(x,0). \tag{B.4}$$

Moreover, both α and β are small values compared to $D_{\rm c}$ and $B_{\rm c}$ respectively. Note that when α and β are exactly zeros, the first term in (B.4) becomes $f\left[B_{\rm c} - f\left[D_{\rm c}\right]\right] = f(B_{\rm c} - A_{\rm c}) = f(D_{\rm c}) = A_{\rm c}$. In addition, since we have $\delta\tau \approx 2\delta A$ near $D_{\rm c}$, the critical value [1], we may simplify

$$\alpha \approx \frac{1}{2}\delta\tau + b - a. \tag{B.5}$$

We now define a function

$$F(u, v) := f(v - f(u)). \tag{B.6}$$

It is obvious that $F(D_c, B_c) = A_c$. Thus by a Taylor series approximation of (B.4) through cubic terms we find

$$\begin{array}{rl} & F(D_c + \alpha, B_c + \beta) \\ = & A_c + F_u \cdot \alpha + F_v \cdot \beta + \dfrac{1}{2}F_{uu} \cdot \alpha^2 + F_{uv} \cdot \alpha\beta + \dfrac{1}{2}F_{vv}\beta^2 \\ & + \dfrac{1}{6}F_{uuu} \cdot \alpha^3 + \dfrac{1}{2}F_{uuv} \cdot \alpha^2\beta + \dfrac{1}{2}F_{uvv}\alpha\beta^2 + \dfrac{1}{6}F_{vvv}\beta^3 \\ & + \text{h.o.t.}, \end{array} \tag{B.7}$$

where all the partial derivatives are taken at the critical point (D_c, B_c) and h.o.t.(higher order terms) means terms of order 4 or higher. By the definition of function $F(u, v)$ in (B.6), we find the partial derivative functions of $F(u, v)$ as listed in Table B.1. Evaluating the partial derivatives in Table B.1 at $(D_{\rm c}, B_{\rm c})$, we obtain

$$\begin{array}{l} F_u = -1, \quad F_v = 1, \quad F_{uu} = 0, \quad F_{uv} = -p_2, \quad F_{uu} = p_2, \\ F_{uuu} = -2p_3 + 3p_2^2, \quad F_{uuv} = p_3 - p_2^2, \quad F_{uvv} = -p_3, \quad F_{vvv} = p_3, \end{array} \tag{B.8}$$

where for convenience we let

$$p_2 = f''(D_c) \quad \text{and} \quad p_3 = f'''(D_c), \tag{B.9}$$

Equation (1.27) implies

$$A(x, 0) = A_c + \delta A + a. \tag{B.10}$$

[1] The restitution curve $A = f(D)$ has the critical value at $D_{\rm c}$, where $f'(D_{\rm c}) = 1$, thus a perturbation of D about $D_{\rm c}$ yeilds $\delta A \approx \delta D$ and so forth $\delta\tau = \delta A + \delta D \approx 2\delta A$.

Table B.1: Partial derivative functions of $F(u,v)$.

$F(u,v)$	$=$	$f(v-f(u))$
$\partial_u F(u,v)$	$=$	$-f'(v-f(u))\cdot f'(u)$
$\partial_v F(u,v)$	$=$	$f'(v-f(u))$
$\partial_{uu} F(u,v)$	$=$	$f''(v-f(u))\cdot f'(u)^2 - f'(v-f(u))f''(u)$
$\partial_{uv} F(u,v)$	$=$	$-f''(v-f(u))\cdot f'(u)$
$\partial_{vv} F(u,v)$	$=$	$f''(v-f(u))$
$\partial_{uuu} F(u,v)$	$=$	$-f'''(v-f(u))f'(u)^3 + 3f''(v-f(u))f'(u)f''(u) - f'(v-f(u))f'''(u)$
$\partial_{uuv} F(u,v)$	$=$	$f'''(v-f(u))f'(u)^2 - f''(v-f(u))f''(u)$
$\partial_{uvv} F(u,v)$	$=$	$-f'''(v-f(u))f'(u)$
$\partial_{vvv} F(u,v)$	$=$	$f'''(v-f(u))$

Substituting (B.7), (B.8) and (B.10) into (B.4), we find that disregarding the higher order terms in (B.7), equation (1.36) can be written in the following form :

$$\begin{aligned} 2B\partial_t a \;&\approx -a - \delta A - \alpha + \beta - p_2\alpha\beta + \frac{1}{2}p_2\beta^2 \\ &\quad + \frac{1}{6}(-2p_3 + 3p_2^2)\alpha^3 + \frac{1}{2}(p_3 - p_2^2)\alpha^2\beta + \frac{1}{2}(-p_3)\alpha\beta^2 + \frac{1}{6}p_3\beta^3. \end{aligned} \tag{B.11}$$

Equation (1.38) is then obtained from approximating (B.11) to leading order under the assumption that the magnitude of $b(x,t)$ is much less than the magnitude of $a(x,t)$ and also $\delta\tau$. We show the details as follow.

Substituting (B.3) and (B.5) into (B.11), we find

$$\begin{aligned} &B\partial_t a \\ &= -b + \frac{1}{4}p_2\beta(\beta - 2\alpha) - \frac{1}{4}p_2^2\alpha^2(\beta - \alpha) + \frac{1}{12}p_3(\beta - 2\alpha)(\beta^2 - \beta\alpha + \alpha^2) + \text{h.o.t.} \\ &\approx -b + \frac{1}{4}p_2(\delta\tau - b)(2a - 3b) - \frac{1}{4}p_2^2\Big(a - 2b + \frac{\delta\tau}{2}\Big)\Big(a - b - \frac{\delta\tau}{2}\Big)^2 \\ &\quad + \frac{1}{12}p_3(2a - 3b)\Big[a^2 - 3ab + \Big(3b^2 - \frac{3\delta\tau}{2}b + \frac{3\delta\tau^2}{4}\Big)\Big] + \text{h.o.t..} \end{aligned} \tag{B.12}$$

Now $b(x,t)$ is assumed to be much less than $a(x,t)$ and also $\delta\tau$. Thus to lowest order,

we may disregard all higher order terms of b in (B.12), i.e. all the terms involving b are disregarded except the term $-b$. We also assume $\delta\tau$ is much less than a. We all the above assumptions, to the lowest order, (B.12) may be reduced to

$$B\partial_t a(x,t) \approx \frac{1}{2}p_2\delta\tau \cdot a - \left(\frac{1}{4}p_2^2 - \frac{1}{6}p_3\right) \cdot a^3 - b. \tag{B.13}$$

Substituting (B.9), the definition for p_2 and p_3, and (1.34), the relationship between a and b, into (B.13) we obtain the equation (1.37), with two constants σ and g defined in (1.38) and (1.39).

Bibliography

[1] R. R. Aliev and A. V. Panfilov. A simple two-variable model of cardiac excitation. *Chaos, Solitons, Fractals*, 7:293–301, 1996.

[2] K. T. Alligood, T. D. Sauer, and J. A. Yorke. *Chaos.* Springer-Verlag, New York, 2000.

[3] S. Alonso, F. Sagués, and A. S. Mikhailov. Taming winfree turbulence of scroll waves in excitable media. *Science*, 299:1722–1725, 2003.

[4] M. Beck, D. G. Schaeffer C. K. R. T. Jonesy, and M. Wechselberger. Electrical waves in a one-dimensional model of cardiac tissue. Submitted to *SIAM J. Appl. Dyn. Syst.*, 2007.

[5] G. W. Beeler and H. Reuter. Reconstruction of the action potential of ventricular myocardial fibers. *J. Physiol.*, 268:177–210, 1977.

[6] J. Cain and D. G. Schaeffer. Two-term asymptotic approximation of a cardiac restitution curve. *SIAM Review*, 48(3):537–546, 2006.

[7] J. Carr. *Applications of Centre Manifold Theory.* Springer-Verlag, New York, 1981.

[8] D. R. Chialvo, D. C. Michaels, and J. Jalife. Supernormal excitability as a mechanism of chaotic dynamics of activation in cardiac purkinje fibers. *Circ. Res.*, 66:525–545, 1990.

[9] D. R. Chialvo, D. C. Michaels, and J. Jalife. Supernormal excitability as a mechanism of chaotic dynamics of activation in cardiac purkinje fibers. *Circ. Res.*, 66:525–545, 1990.

[10] M. Courtemanche, L. Glass, and J. P. Keener. Instabilities of a propagating pulse in a ring of excitable media. *Phys. Rev. Lett.*, 70:2182–2185, 1993.

[11] B. Echebarria and A. Karma. Instability and spatiotemporal dynamics of alternans in paced cardiac tissue. *Phys. Rev. Lett.*, 88:208101, 2002.

[12] B. Echebarria and A. Karma. Amplitude-equation approach to spatiotemporal dynamics of cardiac alternans. *Phys. Rev. E*, 76:051191, 2007.

[13] V. Elharrar and B. Surawicz. Cycle length effect on restitution of action potential duration in dog cardiac fibers. *Am. J. Physiol.*, 244:H782–H792, 1983.

[14] L. C. Evans. *Partial Differential Equations*. American Mathematical Society, Rhode Island, USA, 2000.

[15] F. Fenton and A. Karma. Vortex dynamics in three-dimensional continuous myocardium with fiber rotation: Filament instability and fibrillation. *Chaos*, 8:20–47, 1998.

[16] R. FitzHugh. Thresholds and plateaus in the hodgkinchuxley nerve equations. *J. Gen. Physiol.*, 43:867–896, 1960.

[17] R. FitzHugh. Impulses and physiological states in theoretical models of nerve membrane. *Biophys. J.*, 1:445–466, 1961.

[18] D. Di Francesco and D. Noble. A model of the cardiac electrical activity incorporating ionic pumps and concentration changes - simulations of ionic currents and concentration changes. *Phil. Trans. R. Soc. Lond. B*, 307:353–398, 1985.

[19] P. Fredeiuckson, J. L. Kaplan, E. D. Yorke, and J. A. Yorke. The liaponuv dimension of strange attractors. *J. Diff. Eqn.*, 49:185–207, 1983.

[20] A. Garfinkel, Y.-H. Kim, O. Voroshilovsky, Z. Qu, J. R. Kil, M. Hyoung, H. S. Karagueuzian, J. N. Weiss, and P.-S. Chen. Preventing ventricular fibrillation by flattening cardiac restitution. *Proc. Natl. Acad. Sci. USA*, 97:6061–6066, 2000.

[21] D. B. Geselowitz and W. T. III Miller. A bidomain model for anisotropic cardiac muscle. *Ann. Biomed. Eng.*, 11:191–200, 1983.

[22] M. Golubitsky and D. G. Schaeffer. *Singularities and Groups in Bifurcation Theory*. Springer-Verlag, New York, 1985.

[23] J. Guckenheimer. On a codimension two bifurcation. *Lecture Notes in Mathematics*, 898:99–142, 1981.

[24] J. Guckenheimer and P. Holmes. *Nonlinear Oscillations, Dyanamical Systems, and Bifurcations of Vector Fields*. Springer-Verlag, New York, 1983.

[25] M. R. Guevara, G. Ward, A. Shie, and L. Glass. Electrical alternans and period doubling bifurcations. In *IEEE Computers in Cardiology*, pages 167–170, 1984.

[26] A. Hodgkin and A. Huxley. A quantitative description of membrane current and its application to conduction and excitation in nerve. *J. Physiol.*, 117:500–544, 1952.

[27] P. Holmes. Unfolding a degenerate nonlinear oscillator: a codimension two bifurcation. *Ann. N. Y. Acad. Sci.*, 357(1):473–488, 1980.

[28] R. H. Hoyt, M. L. Cohen, and J. E. Saffitz. Distribution and three-dimensional structure of the intercellular junctions in canine myocardium. *Cir. Res.*, 64:563–574, 1989.

[29] V. Iyer, R. Mazhari, and R. L. Winslow. A computational model of the human left ventricular epicardial myocyte. *Biophys. J.*, 87:1507–1525, 2004.

[30] J. L. Kaplan and J. A. Yorke. Chaotic behavior of multidimensional difference equations. *Lecture Notes in Mathematics*, 730:204–227, 1979.

[31] A. Karma. Spiral breakup in model equations of action potential propagation in cardiac tissue. *Phys. Rev. Lett.*, 71(7):1103–1106, 1993.

[32] Kato. *Perturbation Theory for Linear Operators*. Springer-Verlag, New York, 1966.

[33] J. P. Keener and J. Sneyd. *Mathematical Physiology*. Springer-Verlag, New York, 1998.

[34] W. F. Langford. Periodic and steady state interactions lead to tori. *SIAM J. Appl. Math.*, 37:22–48, 1979.

[35] F. Ledrappier and L. S. Young. Dimension formula for random transformations. *Comm. Math. Phys.*, 117:529–548, 1988.

[36] C. H. Luo and Y. Rudy. A model of the ventricular cardiac action potential, depolarization, repolarization and their interaction. *Circ. Res.*, 68:1501–1526, 1991.

[37] C. H. Luo and Y. Rudy. A dynamic model of the cardiac ventricular action potential. i. simulations of ionic currents and concentration changes. *Circ. Res.*, 74:1071–1096, 1994.

[38] A. Mahajan, Y. Shiferaw, D. Sato, A. Baher, R. Olcese, L.-H. Xie, M.-J. Yang, P.-S. Chen, J. G. Restrepo, A. Karma, A. Garfinkel, Z. Qu, and J. N. Weiss. A rabbit ventricular action potential model replicating cardiac dynamics at rapid heart rates. *Biophys. J.*, 94(2):392–410, 2008.

[39] L. Makowski, D. L. D. Caspar, W. C. Phillips, and D. A. Goodenough. Gap junctional structures ii, analysis of x-ray diffraction. *J. Cell. Bio*, 74:629–654, 1977.

[40] J. Malmivuo and R. Plonsey. *Bioelectromagnetism: Principles and Applications of Bioelectric and Biomagnetic Fields*. Oxford University Press, New York and Oxford, 1995.

[41] R. E. McAllister, D. Noble, and R. W. Tsien. Reconstruction of the electrical activity of cardiac purkinje fibres. *J. Physiol.*, 251:1–59, 1975.

[42] N. Metropolis, M. L. Stein, and P. R. Stein. On finite limit sets for transformations on the unit interval. *J. Combin. Theor.*, 15(A):25–44, 1973.

[43] C. C. Mitchell and D. G. Schaeffer. A two-current model for the dynamics of cardiac membrane. *Bull. Math. Bio.*, 65:767–793, 2003.

[44] J. Nagumo, S. Arimoto, and S. Yoshizawa. An active pulse transmission line simulating nerve axon. *Proc. IRE*, 50:2061–2070, 1962.

[45] D. Noble. A modification of the hodgkin-huxley equations applicable to purkinje fiber actoin and pacemaker potential. *J. Physiol.*, 160:317–352, 1962.

[46] J. B. Nolasco and R. W. Dahlen. A graphic method for the study of alternation of cardiac action potentials. *J. Appl. Physiol.*, 25:191–196, 1968.

[47] E. Ott. *Chaos in dynamical systems, Second Edition*. Cambridge University Press, Cambridge, UK, 2002.

[48] R. Pandit, A. Pande, S. Sinha, and A. Sen. Spiral turbulence and spatiotemporal chaos: Characterization and control in two excitable media. *Physica A*, 360:211–219, 20023.

[49] A. V. Panfilov. Spiral breakup as a model of ventricular fibrillation. *Chaos*, 8:57–64, 1998.

[50] T. S. Parker and L. O. Chua. *Practical numerical algorithms for Chaotic Systems*. Springer-Verlag, New York, 2000.

[51] Jr. R. F. Gilmour and D. R. Chialvo. Electrical restitution, critical mass, and the riddle of fibrillation. *J. Cardiovasc. Electrophysiol.*, 10:1087–1089, 1999.

[52] D. G. Schaeffer, J. Cain, D. Gauthier, S. Kalb, W. Krassowska, R. Oliver, E. Tolkacheva, and W. Ying. An ionically based mapping model with memory for cardiac restitution. *Bull. Math. Bio.*, 69:459–482, 2007.

[53] Y. Shiferaw, M. A. Watanabe, A. Garfinkel, and J. N. Weissand A. Karma. Model of intracellular calcium cycling in ventricular myocytes. *Biophys. J.*, 85:3666–3686, 2003.

[54] Heart Rhythm Society. Sudden cardiac death. *online article at http://www.hrspatients.org/patients/heart_disorders/cardiac_arrest/.*

[55] S. H. Strogatz. *Nonlinear dynamics and chaos: with applications to physics, biology, chemistry, and Engineering*. Springer-Verlag, New York, 2000.

[56] J. Sundnes, G. T. Lines, X. Cai, B. F. Nielsen, K.-A. Mardal, and A. Tveito. *Computing the Electrical Activity in the Heart*. Springer-Verlag, New York, 2006.

[57] J. Sundnes1, B. F. Nielsen1, K. A. Mardal, X. Cai, G. T. Lines, and A. Tveito. On the computational complexity of the bidomain and the monodomain models of electrophysiology. *Ann. Biomed. Eng.*, 34(7):1088–1097, 2006.

[58] A. Vinet. Quasi-periodic movement in a ring model of cardiac tissue: Mulitstability and low dimensional equivalence. *Ann. Biomed. Eng.*, 28:704–720, 2000.

[59] American Heart Association website: http://www.americanheart.org/.

[60] J. N. Weiss, A. Garfinkel, H. S. Karagueuzian, Z. Qu, and P.-S. Chen. Chaos and the transition to ventricular fibrillation: a new approach to antiarrhythmic drug evaluation. *Circulation*, 99:2819–2826, 1999.

[61] R. L. Winslow, J. Rice, S. Jafri, E. Marbán, and B. O'Rourke. Mechanisms of altered excitation-contraction coupling in canine tachycardia-induced heart failure, ii : Model studies. *Circ. Res.*, 84:571–586, 1999.

[62] L. S. Young. Dimension, entropy and lyapunov exponents. *Ergodic Theory and Dyn. Systems*, 2:109–124, 1982.

Biography

Shu Dai was born on June 4, 1980 in Hai'an, Jiangsu Province of China. He received a B.S. in Physics from University of Science and Technology of China in 2000, an M.S. in Physics from University of Science and Technology of China in 2004, an M.A. in Mathematics from Duke University in 2005. He came to Duke University in 2004 and worked with Professor David G. Schaeffer. His article "Spectrum of a linearized amplitude equation for alternans in a cardiac fiber" was published on SIAM J. Appl. Math. 69(3):2008, 704-719, "Bifurcations in a modulation equation for alternans in a cardiac fiber" has been submitted, and "Chaos in one-dimensional cardiac models" is in preparation. He will start postdoctoral work at Mathematical Biosciences Institute at The Ohio State University.